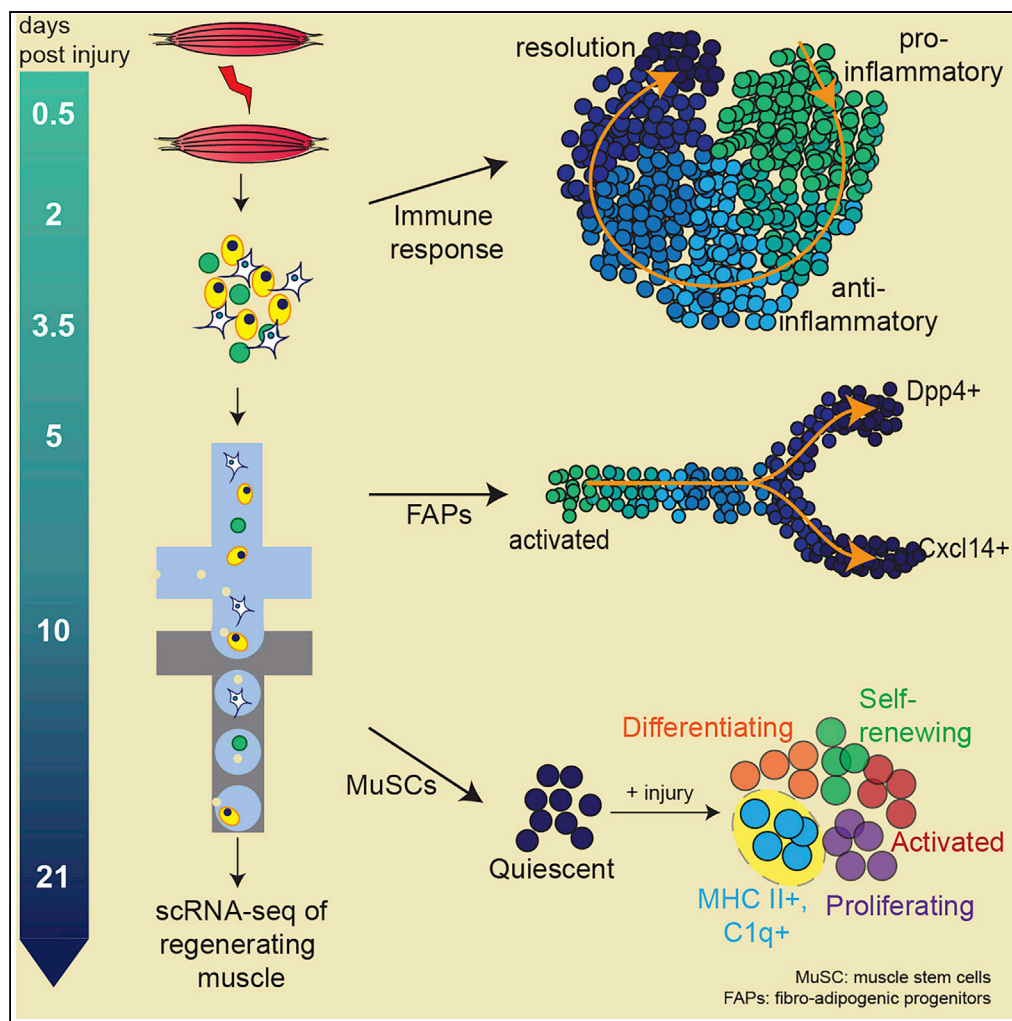## Article

Temporal Dynamics and Heterogeneity of Cell Populations during Skeletal Muscle Regeneration

Stephanie N. Oprescu, Feng Yue, Jiamin Qiu, Luiz F. Brito, Shihuan Kuang

skuang@purdue.edu

HIGHLIGHTS

scRNA-seq of 53,000 cells reveals known and new cell subsets in regenerating muscle

Immune cells exhibit early infiltration, pro- and anti-inflammation and slow resolution

Linear trajectory of activated FAPs to Dpp4+ and Cxcl14+ cells in non-injured muscle

A subset of MuSCs enriched for immune gene expression in regenerating muscle

DATA AND CODE AVAILABILITY

GSE138826

Article

Temporal Dynamics and Heterogeneity of Cell Populations during Skeletal Muscle Regeneration

Stephanie N. Oprescu,[1] Feng Yue,[2] Jiamin Qiu,[2] Luiz F. Brito,[2] and Shihuan Kuang[1,2,3,4,*]

SUMMARY

Mammalian skeletal muscle possesses a unique ability to regenerate, which is primarily mediated by a population of resident muscle stem cells (MuSCs) and requires a concerted response from other supporting cell populations. Previous targeted analysis has described the involvement of various specific populations in regeneration, but an unbiased and simultaneous evaluation of all cell populations has been limited. Therefore, we used single-cell RNA-sequencing to uncover gene expression signatures of over 53,000 individual cells during skeletal muscle regeneration. Cells clustered into 25 populations and subpopulations, including a subpopulation of immune gene enriched myoblasts (immunomyoblasts) and subpopulations of fibro-adipogenic progenitors. Our analyses also uncovered striking spatiotemporal dynamics in gene expression, population composition, and cell-cell interaction during muscle regeneration. These findings provide insights into the cellular and molecular underpinning of skeletal muscle regeneration.

INTRODUCTION

Tissue regeneration is a necessary process that allows damaged tissues to repair and remodel upon injury. Mammalian tissue regeneration is restricted to a subset of tissues, and incomplete repair can lead to scar formation or fibrotic deposition (Cordero-Espinoza and Huch, 2018; Larouche et al., 2018; Moyer and Wagner, 2011; Wynn and Vannella, 2016). Therefore, it is critical to understand the cell types and processes that mediate tissue healing in order to improve regenerative efficiency while limiting scar formation. Although regeneration is a complex and regulated process, skeletal muscle harbors a well-studied population of stem cells that supports its regenerative capacity (Yin et al., 2013). As such, skeletal muscle is an ideal tissue to investigate mechanisms underlying successful regeneration toward improving stem-cell-based therapies.

Skeletal muscle is composed of multinucleated mature muscle cells (myofibers), a resident pool of muscle stem cells (MuSCs, also called muscle satellite cells), and other populations such as fibro-adipogenic progenitors (FAPs), endothelial cells, tenocytes, and resident immune cells (Paylor et al., 2011). Upon injury, MuSCs activate, proliferate, differentiate, and fuse together to repair damaged myofibers. However, their appropriate responses are mediated by both resident and infiltrating cells (Paylor et al., 2011; Relaix and Zammit, 2012). Immediately after injury, neutrophils and macrophages invade the damaged tissue and sustain a pro-inflammatory environment to help clear necrotic tissue (Juhas et al., 2018; Lu et al., 2011). The pro-inflammatory environment sustains MuSC proliferation, whereas the anti-inflammatory environment allows for MuSC differentiation, providing synergism between the immune and stem cell responses (Arnold et al., 2007; Deng et al., 2012; Villalta et al., 2011). For example, anti-inflammatory macrophages couple angiogenesis with MuSC differentiation through the production of oncostatin M, underscoring the interdependence of various cellular responses (Christov et al., 2007; Latroche et al., 2017; Arnold et al., 2007; Burzyn et al., 2013; Hardy et al., 2016; Heredia et al., 2013; Joe et al., 2010; Segawa et al., 2008; Tidball and Wehling-Henricks, 2007). These and many other studies emphasize the importance of MuSCs, supporting cell types and intercellular communication networks for successful muscle regeneration. However, conventional research has relied on targeted approaches to evaluate population-specific characteristics and thus has not provided a full picture of the events and dynamics.

Single-cell RNA-sequencing (scRNA-seq) provides the opportunity to deconvolute heterogeneous tissue into individual cells based on their transcriptomic profiles (Hwang et al., 2018). In combination with various computational techniques, scRNA-seq has revolutionized our understanding of tissue function and

[1]Department of Biological Sciences, Purdue University, 915 W State St, West Lafayette, IN 47907, USA

[2]Department of Animal Sciences, Purdue University, 270 S Russell St, West Lafayette, IN 47907, USA

[3]Center for Cancer Research, Purdue University, 201 S University St, West Lafayette, IN 47907, USA

[4]Lead Contact

*Correspondence:
skuang@purdue.edu

exposed a tremendous amount of heterogeneity in homeostatic tissues (Zeng and Dai, 2019; Zilionis et al., 2019). For example, scRNA-seq has provided insights about the regeneration program in axolotl, identified an interstitial fat progenitor population in both mouse and human adipose tissue, and demonstrated the similarity of infiltrating myeloid cells in human and mouse lung cancer (Gerber et al., 2018; Merrick et al., 2019; Zilionis et al., 2019). scRNA-seq has been used to describe cell-cell communication networks within tumor microenvironments, small intestinal crypts, mouse bone marrow, and across liver endothelial cells, emphasizing the breadth of information that can be gained to understand the cellular and molecular regulation of tissue homeostasis and diseases (Boisset et al., 2018; Halpern et al., 2018; Kumar et al., 2018).

Recent scRNA-seq studies on mouse hindlimb muscle identified a new population of interstitial tenocytes that function during muscle repair and defined distinct transcriptional programs in quiescent and activated MuSCs (Dell'orso et al., 2019; Giordani et al., 2019). scRNA-seq on muscle FAPs during mouse development, regeneration, and from a Duchenne's muscular dystrophy model suggest that a Vcam1-positive FAP population underlies fibrotic persistence (Malecova et al., 2018). A recent publication highlighted the transcriptional diversity of cells from muscle organoids and outlined growth factors required for MuSC differentiation in organoid culture (Wang et al., 2018), whereas two recent pre-prints employed scRNA-seq to study cell-type-specific responses to muscle injury at 2, 4, 5, and 7 days post injury (Micheli et al., 2019; Pawlikowski et al., 2019). However, a comprehensive characterization from the immediate response through to near pre-injury levels has not been described at the single-cell transcriptomic level.

We employed scRNA-seq of skeletal muscle to understand the transcriptional dynamics that underpin muscle regeneration at six key regenerative time-points and in non-injured muscle. We selected early time points to capture the immediate cellular responses and later time points during muscle maturation and recovery to provide the most comprehensive scRNA-seq analysis of muscle regeneration to date. Our findings highlight the continuous transition of immune populations and suggest that two unique FAP populations are present in resting, non-injured muscle that adopt distinct transcriptional features immediately upon injury. We also identify a unique subpopulation of MuSCs enriched for immune-related transcripts and outline potential receptor-ligand pairs to identify key players in cell-communication networks during muscle regeneration. Our findings provide insights into muscle regeneration and serve as a foundation for future exploration of the potentially critical role of various cellular populations and subpopulations in effective skeletal muscle repair.

RESULTS

scRNA-Seq Reveals Transcriptional Dynamics during Muscle Regeneration

To understand cellular dynamics and interactions during muscle regeneration, we performed scRNA-seq of single cell suspensions collected at various stages of muscle regeneration (summarized in Figure S1A). Time points were selected based on the published literature in an effort to capture cell-type heterogeneity. Specifically, we chose 0.5, 2, 3.5, and 5 days post injury (DPI) as these stages are highly dynamic, involve an immediate immune response, and yield progressive changes that support MuSC activation, proliferation, and differentiation into newly regenerated fibers (Arnold et al., 2007; Deng et al., 2012; Garry et al., 2016; Lu et al., 2011; Relaix and Zammit, 2012). We also analyzed muscles at 10 DPI, when the degenerated myofibers are largely regenerated, and 21 DPI, when regeneration is assumed to be nearly complete and muscle function recovered (Baghdadi and Tajbakhsh, 2018). We also evaluated the morphological features of these time points by histological sectioning (Figure S1B), to confirm that these time points would best capture regeneration dynamics using scRNA-seq.

To generate single-cell suspensions for scRNA-seq, tibialis anterior (TA) muscles were isolated from non-injured and injured mice at six regenerative time points (n = 3 mice per time point, pooled into one sample) for cell isolation. Fluorescence-activated cell sorting (FACS) was then used to select for single cells and exclude aggregated cells, dead cells, and debris (Figure S1C; detailed in Transparent Methods). The 10X Genomics Chromium Platform was used to generate single cell libraries, which were processed according to the manufacturer's instructions and sequenced on an Illumina NovaSeq platform. Individual cells were filtered based on mitochondrial RNA content, features, and reads/cell to yield a total of 53,193 cells across the seven samples with an average of 7,599 cells/sample (Figure S2). Since the seven samples were processed in four batches, we used principal-component analysis (PCA) to determine if batch effects contributed to the variance across samples (Figure S3). As these results did not suggest that samples
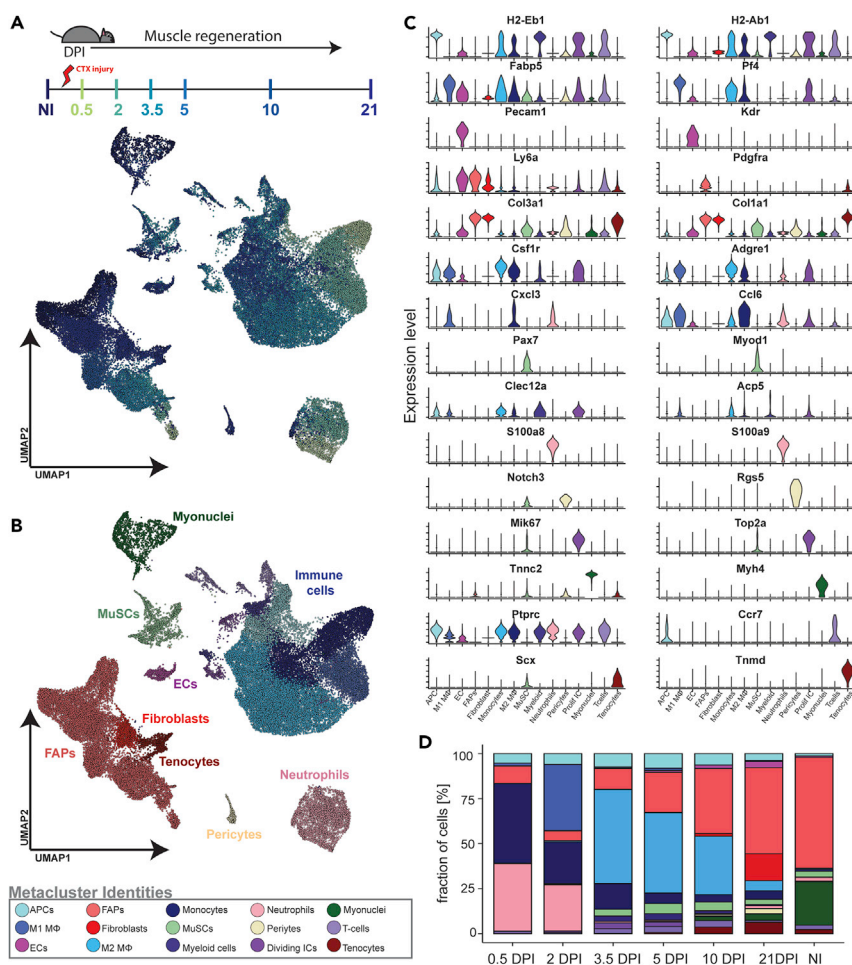
Figure 1. Single-Cell RNA Profiling of Over 53,000 Cells during Skeletal Muscle Regeneration

(A) Single-cell suspensions were generated from non-injured whole tibialis anterior muscle and six time points following injury with cardiotoxin (CTX). UMAP embedding of scRNA-seq data colored by time point highlights the progressive nature of skeletal muscle regeneration. The regeneration time point color correlates with the timeline scheme.

(B) UMAP embedding of scRNA-seq data colored by meta-clusters to simplify visualization.

(C) Violin plots grouped by meta-clusters demonstrate cell-type marker gene expression, which was used to classify meta-clusters.

(D) Relative proportion of cell types at each time point. Shows initial abundance of inflammatory immune cells and gradual decrease of immune cell abundance with a concurrent increase in FAP populations. Regeneration time point plotted along x axis, relative abundance as a % of total cells along the y axis. Abbreviations: APC, antigen-presenting cells; CTX, cardiotoxin; DCs, dendritic cells; Dividing IC, dividing immune cells; DPI, days post injury; ECs, endothelial cells; FAPs, fibro-adipogenic progenitors; MΦ, macrophages; MuSCs, muscle satellite cells; NI, non-injured.

were purely separated by batch, we combined all cells from the seven samples and performed unsupervised clustering and UMAP embedding using the Seurat R package (Butler et al., 2018).

UMAP embedding of all seven samples colored by time point highlighted the progressive nature of muscle regeneration (Figure 1A). Unsupervised clustering identified a total of 25 clusters across the seven time-points (Figures S4 and S5), which we manually grouped into meta-clusters based on marker gene expression to simplify visualization (Figures 1B and 1C). MuSCs, pericytes, endothelial cells, and myonuclei all formed discrete clusters (Figure 1B). Immune cells formed several discrete clusters including neutrophils, T-cells, and a large cluster of cells containing eleven subpopulations (Figure S4). Similarly, a population of mesenchymal cells containing fibroblasts, tenocytes, and fibro-adipogenic progenitors (FAPs) formed eight clusters (Figure S4), which we henceforth refer to as FAPs for simplicity. The cell populations identified

are consistent with the previously published literature (Baghdadi and Tajbakhsh, 2018), suggesting our data recapitulated key events involved in regeneration.

In non-injured muscle, the primary cell types identified were FAPs and myonuclei (which were presumably released during tissue mincing and digestion and isolated by FACS as single cells), accounting for 62% and 24% of the total population, respectively (Figure 1D). MuSCs comprised 3.1% of the total cell populations, and immune cells made up 7% (Figure 1D). Immediately after injury, immune cells accounted for 87% of the total fraction of cells, whereas the abundance of FAPs dropped to 10% (Figure 1D), highlighting the immediate cell-type response to muscle injury. Few MuSCs were detected by scRNA-seq at 0.5 and 2 DPI, although they were readily detected in cross sections (Figure S6). This may be due to inefficient digestion/isolation of highly inflammatory muscle tissue at these early time points (Goodyear et al., 2014; Trapecar et al., 2017). Nonetheless, MuSCs were readily detectable (3.8%) by 3.5 DPI, along with an increased abundance of FAPs and shifts in the immune cell types (Figure 1D). Consistent with the ongoing resolution of muscle injury, the relative fraction of immune cells began to decline by 5 DPI, whereas the relative fraction of FAPs increased through 21 DPI (Figure 1D). A simple comparison of the transcriptional features from non-injured and 21 DPI also suggested that muscle-specific transcripts were enriched in non-injured compared with 21 DPI, whereas *Col1a1* appeared to be enriched at 21 DPI compared with non-injured (Figure S7). This may indicate on-going fibrosis and tissue remodeling at 21 DPI that has not resolved to pre-injury levels. In summary, these data highlight the progressive nature of muscle regeneration and represent the largest scRNA-seq profile of muscle regeneration to date.

Profiling of Immune Cells Reveals a Dynamic and Progressive Immune Response

Immune cells comprised the largest population in our data and displayed the most dynamic, transient, and time-dependent transcriptional features compared with other cell populations. In non-injured muscle, we detected a small population of resident $Cd3^+$ and $Cd4^+$ T cells, as well as small populations of dendritic cells, monocytes, and neutrophils (Figure 2A, vii-viii). Immediately upon injury, leukocytes, M1 macrophages, and neutrophils were the primary cell types detected (Figure 2A, i-ii). Leukocytes were enriched for *Vcan*, *Cxcl3*, and *Chil3*; M1 macrophages expressed *Cd36*, *Arg1*, *Spp1 Fabp4*, and *Fabp5*; and neutrophils specifically expressed *S100a8* and *S100a9* (Figure S5). Neutrophils also expressed *Csf1* at these early regeneration stages, which has been shown to modulate the tissue-resident macrophages' response and thus outlines the progressive inter-cellular communication network (Braza et al., 2018). Nonetheless, these early-stage immune populations were transient and not detected at the subsequent time points.

At 3.5 and 5 DPI, we detected a population of $Il7r^+$ macrophages, M2 macrophages, and $Ly6c^+$ monocytes (Figure 2A and iii-iv). The $Il7r^+$ macrophages expressed *Gpnmb*, *Msrb1*, and *Pld3*; M2 macrophages were enriched for *C1qa*, *C1qb*, *C1qc*, *Ms4a6*, and *Ms4a7*; and $Ly6c^+$ monocytes expressed *Cd52*, *Ccr2*, and *Tlr2*. We also detected a late-stage population of macrophages with M2-like characteristics, which we labeled $Mrc1^+$ macrophages. These macrophages were detected at 5 and 10 DPI and were enriched for *H2-Aa*, *H2-Eb1*, and *H2-Ab1*, as well as markers of immature dendritic cells such as *Tmem176a*, *Tmem176b*, and *Cd81* (Figures 2A and iv-v and S5). T cells were most abundant at 10 and 21 DPI when most myofibers are fully regenerated, suggesting they may play a role in muscle remodeling (Figure 2A and v-vi).

To highlight the gene expression characteristics of the immune response, we analyzed time-point-specific gene expression. These data suggest that the immediate response to muscle injury is governed by a pro-inflammatory phenotype, which subsequently switches to an anti-inflammatory phenotype that yields a gradual resolution (Figures 2B and S8). Chil3, Tnf, Ptgs2, Ccl2, and Cxcl3 have known pro-inflammatory roles and were markedly enriched and specific to 0.5 and 2 DPI (Figure 2B) (Yang and Hu, 2018). Later time-point-specific gene expression characteristics included *Tmem176b*, *Cd74*, *H2-Eb1*, *H2-Aa*, and *Ms4a7* (Figure 2B), which are markers for anti-inflammatory macrophages and dendritic cells in our dataset. The clear switch in gene expression signatures from 2 to 3.5 DPI is consistent with the switch from a pro- to anti-inflammatory immune environment (Figures S8 and 2C) and is nicely recapitulated by the clockwise shift of immune cell types during regeneration. Thus, these data will further serve the community as a tool to explore the immune-cell-specific transcriptional characteristics during muscle regeneration.

Divergence and Bilineage Trajectory of FAP Populations

FAPs reside in the muscle interstitium and play a role in mediating the immune response and ECM remodeling to support skeletal muscle regeneration (Biferali et al., 2019). Based on the expression of *Pdgfra*, *Sca1*,
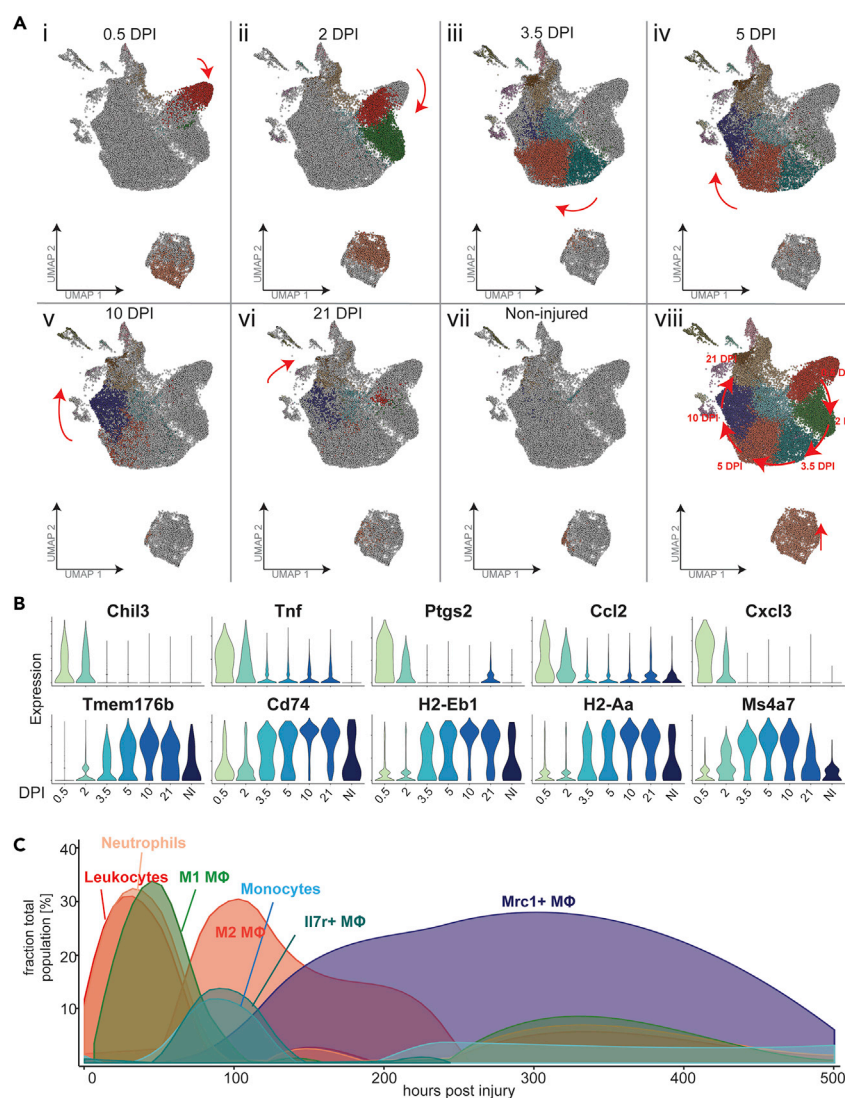
Figure 2. Immune Cell Dynamics during Muscle Regeneration

(A) UMAP embedding of immune cell populations during muscle regeneration, colored by cluster. Panels (i)–(vii) time-point-specific immune cell populations. Arrows drawn to highlight the progressive nature of the immune response and subsequent resolution to near non-injured levels by 21 DPI. Panel (viii) UMAP embedding colored to show all immune cell populations and their cluster identity.

(B) Violin plots showing gene-specific expression trends as a function of regeneration time point. Top panel of violin plots highlights pro-inflammatory gene signatures that are enriched at 0.5 and 2 DPI, whereas the bottom panel shows later-stage anti-inflammatory and antigen presentation gene signatures.

(C) Density plot to demonstrate immune population dynamics throughout the course of regeneration. Immediate response is primarily mediated by pro-inflammatory immune cells such as neutrophils and M1 MΦ's and subsequently followed by anti-inflammatory immune populations. X axis is hours post injury (with 0 being non-injured); along the y axis is fraction of the immune cell population out of total cells per time point, expressed as %. Abbreviations: DPI, days post injury; MΦ, macrophages.

and *Cd34*, we identified a heterogeneous and dynamic cluster of FAPs throughout regeneration (Figures 3A and 3B). Tenocytes marked by the expression of *Tnmd* and *Scx* clustered closely with FAPs, all within the larger mesenchymal cell population (Figure 3B). Unlike the immune population which exhibited a progressive nature to yield a nearly resolved state by 21 DPI, FAP populations followed a linear trajectory emerging from 0.5 DPI. Upon muscle damage, we detected a FAP population with distinct transcriptional characteristics compared with the non-injured populations. We labeled this subpopulation as activated FAPs as they
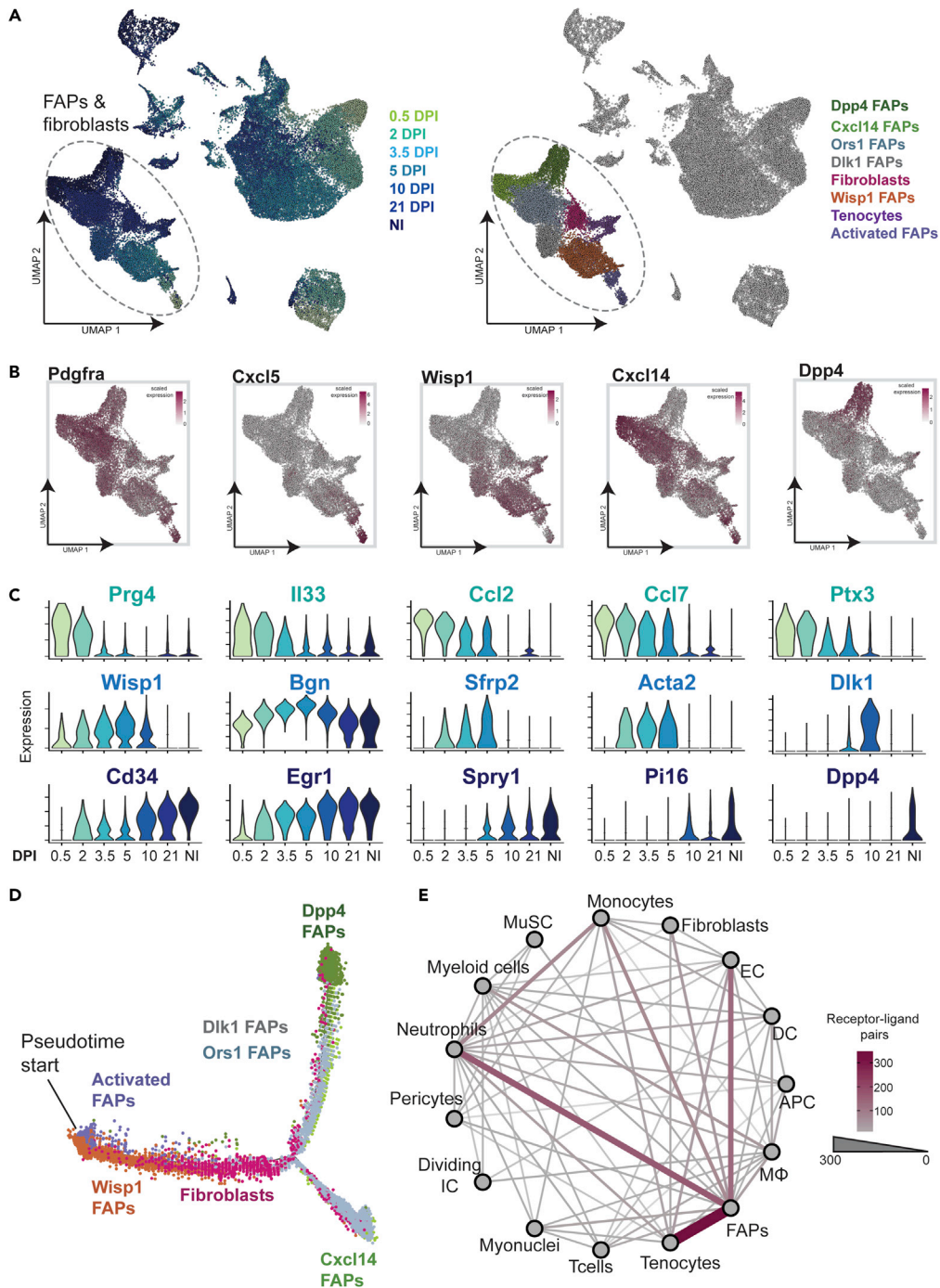
Figure 3. Fibro-Adipogenic Progenitor Population Dynamics during Muscle Regeneration

(A) UMAP embedding of all cells profiled by scRNA-seq during regeneration. Left panel colored by time point, right panel colored by FAP cluster identity. Dotted line circles the FAP population.

(B) Feature plots showing the normalized expression of cluster-specific genes. *Pdgfra* is expressed by most cells, whereas *Cxcl5* is restricted to the activated FAP population. *Wisp1* is expressed mostly in FAPs from 3.5 to 5 DPI, whereas *Cxcl14* and *Dpp4* may represent two divergent FAP subpopulations present in resting, non-injured muscle.

(C) Violin plots of genes exhibiting time-point-specific expression dynamics. The top panel highlights enrichment of immune-modulatory factors at early time points, the middle panel highlights genes enriched at 3.5–10 DPI, whereas the bottom highlights the expression of genes enriched at 21 DPI and in non-injured muscle.

Figure 3. *Continued*

(D) Pseudotime trajectory inference using Monocle of the FAP populations (not including tenocytes). Activated FAPs were selected as the start, and Monocle arranged cells accordingly. UMAP embedding and trajectory inference exhibit a similar pattern in which activated FAPs diverge into two subpopulations present in resting muscle.

(E) Plot to highlight the putative interactome of FAPs, highlighting their diverse role in response to muscle injury. Cell types are grouped by meta-clusters to simplify visualization. Each connection is the sum of interactions across all of the time points.

Abbreviations: APC, antigen-presenting cells; DCs, dendritic cells; Dividing IC, dividing immune cells; DPI, days post injury; ECs, endothelial cells; FAPs, fibro-adipogenic progenitors; MΦ, macrophages; MuSCs, muscle satellite cells; NI, non-injured.

were marked by the expression of *Cxcl5*, *Cxcl3*, *Ccl7*, and *Ccl2* (Figure 3B). Activated FAPs were detected at early regeneration stages (0.5 and 2 DPI) and transitioned into a Wisp1$^+$ FAP subpopulation at 3.5 and 5 DPI (Figure 3B). Wisp1$^+$ FAPs were enriched for ECM-remodeling factors such as *Col8a1*, *Col12a1*, *Col16a1*, *Col11a1*, *Tnc*, *Fbn2*, and *Adam12*. Unique to 10 DPI, we detected a population of Dlk1$^+$ FAPs (Figure 3C) enriched for genes that show complex imprinting patterns such as *B830012L14Rik*, *Meg3*, *Airn*, *Peg3*, *Zim1*, *H19*, and *Igf2* (Ye et al., 2014). Osr1$^+$ FAPs and a fibroblast population (enriched for genes encoding type I collagen) were the primary populations at 21 DPI. Osr1$^+$ FAPs expressed cell-signaling-related genes such as *Ccl1*, *Bmp4*, *Bmp5*, and *Wnt5a*, and interestingly, some of the Osr1$^+$ FAPs diverged into the two populations identified in the non-injured muscle: a Dpp4$^+$ FAP population and a Cxcl14$^+$ FAP population (Figures 3A and 3C). The Dpp4$^+$ FAPs also expressed *Pi16* and *Wnt2*, thus representing the muscle analogue of the reticulum interstitial adipose progenitors recently identified in the adipose tissues (Merrick et al., 2019). The Cxcl14$^+$ FAPs expressed genes encoding secreted enzymes, such as *Enpp2*, *Crispld2*, and *Hsd11b1*. Furthermore, recent scRNA-seq of FAP in muscle identified two similar subpopulations (Scott et al., 2019), further corroborating our data and analysis. To highlight the stage-specific gene expression characteristics, we evaluated markers enriched in the FAP populations by regeneration time point (Figure 3C). Early response genes were implicated in cytokine interactions, whereas the later time points were enriched for ECM factors (Figure 3C), suggesting FAPs may function to mediate immune infiltration and muscle remodeling at early and late regenerative stages, respectively. A gene signature list for the top 50 enriched genes for each subpopulation is provided in Table S2.

The directional progression and divergence of the FAP populations from 0.5 DPI to the two subpopulations detected in non-injured muscle was a unique attribute to this cluster of cells. To determine if these populations may represent transitional states, we employed Monocle for trajectory inference and selected activated FAPs as the start point. Monocle is an unsupervised algorithm that aligns cells along an inferred trajectory and can robustly recapitulate differentiation programs and other biological processes (Trapnell et al., 2014). Monocle arranged FAPs along a common trajectory that diverged into two distinct branches, which coincided with the two subpopulations (Cxcl14$^+$ and Dpp4$^+$) detected in non-injured muscle (Figures 3D and S9A–S9C). Activated and Wisp1$^+$ FAPs localized toward the start of pseudotime, whereas the fibroblasts did not appear to have any spatial bias. Osr1$^+$ and Dlk1$^+$ FAPs were distributed along the two major branches (Figure 3D). Gene expression plots of *Dpp4* and *Cxcl14* highlight the divergent fates the two FAP subpopulations occupy in pseudotime, confirming that Cxcl14+ and Dpp4+ FAPs represent two distinct subpopulations in non-injured muscle (Figure S9C). As the tenocytes represent a relatively well-characterized population distinct from FAPs (Subramanian and Schilling, 2015), they were not included in trajectory analysis. These results were further corroborated by Slingshot, a semi-unsupervised clustering algorithm that uses scRNA-seq data to construct cell lineages and scored highest for accuracy and stability compared with all tree-based inference methods (Saelens et al., 2019; Street et al., 2018). Lineage inference with Slingshot on subclustered and UMAP embedded FAPs similarly produced a trajectory that diverged to yield the Dpp4$^+$ and Cxcl14$^+$ FAPs, consistent with Monocle and the global UMAP structure (Figures S9D–S9F). These results suggest that the FAP populations represent a continuous state during regeneration and may diverge into the Dpp4$^+$ and Cxcl14$^+$ FAP subpopulations present in non-injured muscle.

To better understand the requirement of FAPs, we evaluated the co-enrichment of receptor-ligand pairs across all cells per time point using a published receptor-ligand dataset (Ramilowski et al., 2015). For each time point, we evaluated the expression of receptor-ligand pairs enriched across all cell types and plotted the sum of these interactions to identify which cells may mediate cell-cell communication. Given that tenocytes express high levels of collagen-related genes, we were not surprised to identify a high enrichment of putative interactions among FAPs and tenocytes (Figure 3E). Nonetheless, FAPs were also enriched for putative receptor-ligand pairs across various immune cell types, consistent with their

immunomodulatory and ECM remodeling functions (Figure 3E and Table S3). In sum, these data highlight the diverse and perhaps supportive role for FAPs in muscle regeneration.

MuSC Sub-clustering Reveals a Subpopulation of Myoblasts with Immune Gene Characteristics

MuSCs from all regeneration time points formed a single population distinct from other clusters (Figures 1B and 4A). To better understand the transcriptional features within the MuSC population, we performed unsupervised clustering on the MuSCs containing the transcripts of 1,727 cells. This identified a total of six unique subclusters that we labeled according to their gene expression profiles (Figures 4A and 4B). Specifically, we identified a subpopulation of quiescent MuSCs that expressed *Pax7*, *Sdc4*, *Col3a1*, *Pten*, and *Spry1* (Fukada et al., 2007; Pietrosemoli et al., 2017; Shea et al., 2010; van Velthoven et al., 2017; Yue et al., 2017), which comprised MuSCs mostly from non-injured muscle (Figures 4B, 4C, and S10). Activated MuSCs expressed *Pax7*, *Myod1*, *Islr*, and *Itm2a*, whereas dividing MuSCs also expressed *Pax7* but were enriched for cell-cycle-related genes *Mik67*, *Top2a*, and *Cdk1* (Lagha et al., 2013). The committed and differentiated subpopulations expressed differentiation and mature muscle markers such as *Myogenin*, *Ttn*, *Myh3*, and *Myl4*, with higher expression levels in the differentiated subpopulation. MuSCs from 0.5 to 5 DPI were mostly composed of activated, dividing, committed, and differentiated MuSCs, respectively (Figure S10), consistent with known stages of MuSC-mediated myogenesis in response to injury.

Surprisingly, we also identified an MuSC subpopulation that has not been previously described. This population was enriched for genes involved in immune cell complement activation (*C1qa*, *C1qb*, *C1qc*), major histocompatibility class II antigens (*H2-Eb1*, *H2-Aa*, *H2-Ab1*) and members of the cathepsin family (*Ctsb*, *Ctss*), in addition to the expression of myogenic genes (Figure S10 and Table S4). We therefore coined this subpopulation of MuSCs as immunomyoblasts (IMBs). A small proportion of MuSCs at early regeneration stages fell within this sub-cluster, whereas at 21 DPI nearly 50% of detected MuSCs were immunomyoblasts (Figure 4C). Although this subpopulation had a similar gene expression profile to quiescent, activated, and dividing MuSCs, the expression of immune-related genes was restricted to this population (Figure S10). In summary, a progressive change in gene expression mediates the transition from quiescent to differentiated MuSCs, and our results highlight the robustness of scRNA-seq in recapitulating this dynamic and capture a unique subpopulation of MuSCs that have not been described to date.

Given that our data recapitulated known stages of MuSC transition from quiescence to differentiation, we used Monocle to assess if the IMB subpopulation represents a previously undescribed MuSC fate (Trapnell et al., 2014). Monocle arranged the majority of cells along two trajectories and one smaller trajectory (Figure 4E). Quiescent MuSCs plotted tightly together at the start of pseudotime, whereas activated MuSCs did not exhibit a spatial bias, suggesting that the activation state of MuSCs is continuous. Committed and differentiated MuSCs localized at the two ends of the major branchpoint, whereas dividing cells were restricted to the lower half of the pseudotime space (Figure 4E). This may suggest that MuSCs go from quiescence to activation and then can be fated to (1) differentiate (top right branch) or (2) proliferate and then differentiate (bottom branch furthest to right) or self-renew (bottom branchpoint toward the left) (Figure 4E). Consistent with this notion, *Pax7* and *Cdk1* expression was enriched in the lower half of pseudotime space, whereas *Myog* was restricted to the end of the major branchpoint (top and bottom right branches, Figure S11A). We next plotted the gene expression of markers associated with quiescent and differentiated MuSCs. The expression of quiescent markers was enriched at the start of pseudotime, whereas differentiation markers were enriched at the end (Figure 4F). Also enriched toward the end of pseudotime were cell-cycle-related genes (Figure 4F), which may represent gene expression characteristics of a self-renewing MuSC population. Although immunomyoblasts did not occupy a specific pseudotime space, gene signatures of this population (i.e., *Ctss*, *Ctsb*, *Ms4a7*, *H2-Aa*, *C1qa*, *C1qb*, *C1qc*) were transiently expressed along the progression of pseudotime (Figure 4F), suggesting that this subpopulation may represent a transitional MuSC state. We also used Slingshot to corroborate these findings and selected quiescent MuSCs as the start point and differentiated MuSCs as the endpoint (Figure S11B). Based on the constructed minimum spanning tree (MST), Slingshot identified three distinct lineages in the MuSC cluster that highlight the (1) differentiation trajectory, (2) the dividing trajectory, and (3) the immunomyoblast trajectory (Figure S11B). Genes that defined the immunomyoblast fate highlighted the distinct transcriptional features of this subpopulation and promoted us to further evaluate their expression in MuSCs.
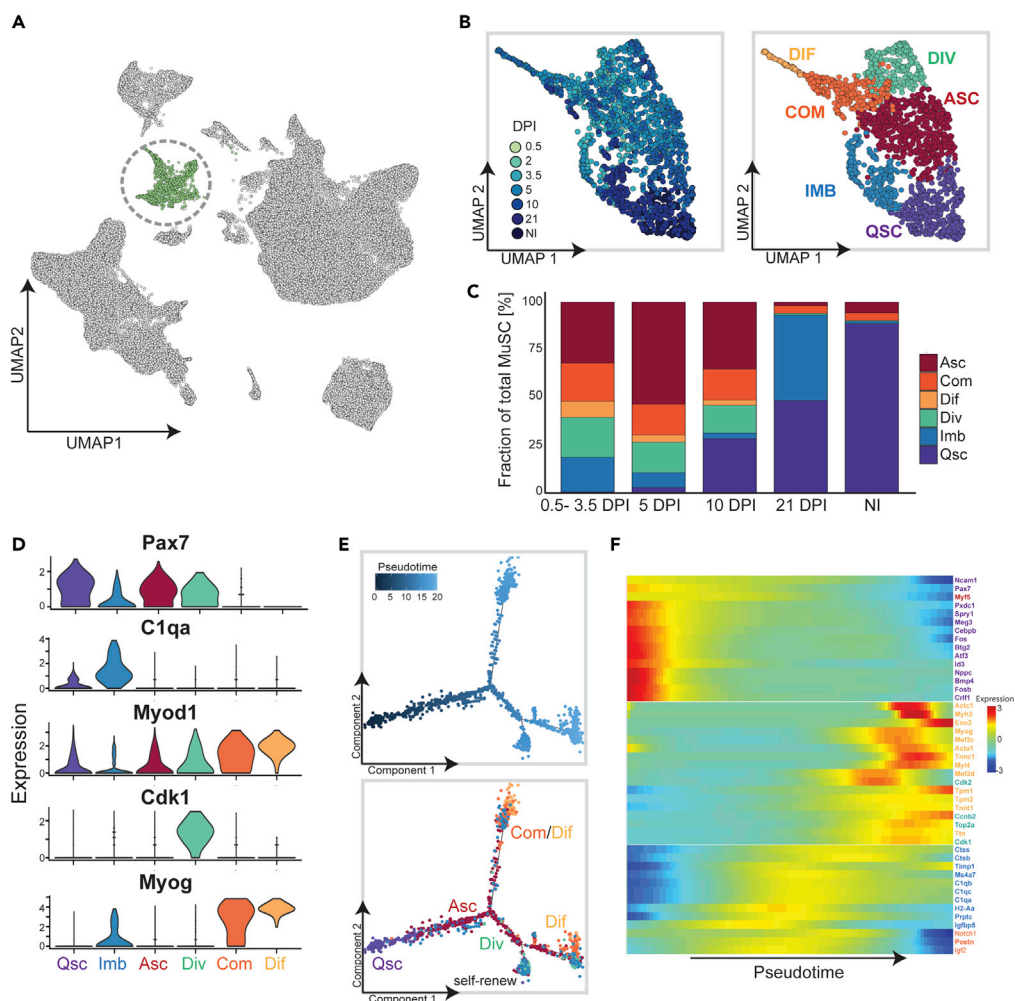
Figure 4. MuSC Sub-cluster Analysis Reveals Subpopulation Enriched for Immune Gene Expression

(A) UMAP embedding of all cells profiled during muscle regeneration. MuSCs are colored in green and circled; all other cells are colored in gray.

(B) Subclustering of MuSCs. Left panel colored by regeneration time point; right panel colored by cluster identity.

(C) Bar graphs to represent the proportion of MuSC subcluster for each time point; 0.5, 2, and 3.5 DPI were combined owing to low number of MuSCs detected at 0.5 and 2 DPI.

(D) Violin plots to show subcluster-specific gene expression and enrichment of C1qa in the immuno-myoblast sub-cluster. Colored by cluster identity.

(E) Pseudotime trajectory inference using Monocle, cells are plotted along the inferred trajectory. Quiescent MuSCs were selected as the start of pseudotime, which is indicated in the top panel. The bottom panel is colored by the cluster identities.

(F) Heatmap of selected genes to show their dynamic expression along pseudotime. Genes enriched in quiescent MuSCs are enriched at the start of pseudotime, whereas differentiation-specific genes are expressed at the end of pseudotime. Gene names are colored by subcluster identity in which they are enriched. Expression values are the log(expression value +0.1). Abbreviations: MuSCs, muscle satellite cells; QSC, quiescent MuSCs; ASC, activated MuSCs; IMB, immuno-myoblasts; DIV, dividing MuSCs; DIF, differentiated MuSCs; COM, committed MuSCs; DPI, days post injury.

As the IMB subpopulation of MuSCs has not been described, we sought to confirm the expression of some of the features uniquely enriched in this population. To this end, we used FACS to isolate MuSCs from non-injured and 5 DPI hindlimb muscles of *Pax7^CreER^:sfGFP* reporter mice, which allowed the conditional labeling of Pax7-positive cells and all of the progeny with nuclear-membrane GFP upon administration of tamoxifen (Figure S12A) (Luo et al., 2017; Murphy et al., 2011). We isolated RNA, generated cDNA, and probed the expression of some of the aforementioned markers enriched in the IMB population identified in our scRNA-seq dataset by RT-PCR. This confirmed that MuSCs isolated from 5 DPI muscle indeed
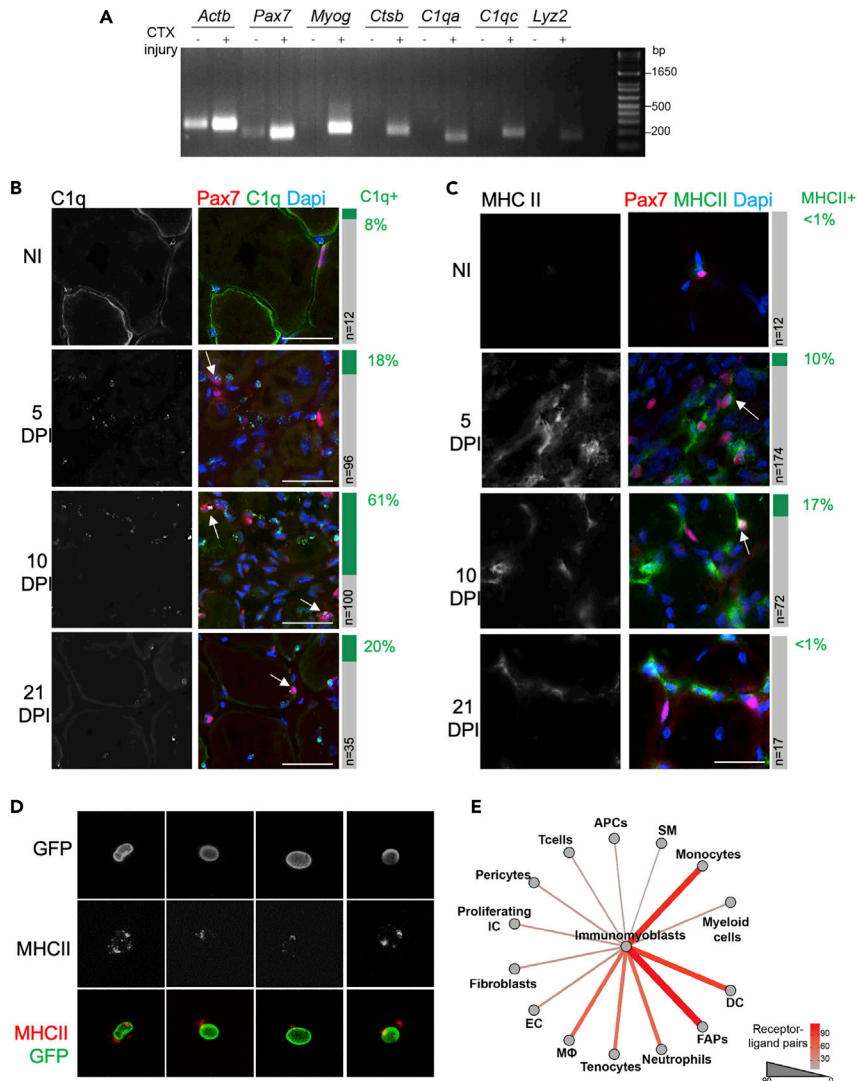
Figure 5. Evaluation of Immune Gene Expression in MuSCs

(A) RT-PCR to detect the expression of immune genes in MuSCs isolated from non-injured muscle (-CTX) or 5 DPI (+CTX). Genes are marked along the top.

(B) Immunofluorescence to detect Pax7 and C1q on sections from non-injured and 5, 10, and 21 DPI TA muscle. Left panel: C1q single channel, right panel: merged. Bar on right: quantification of Pax7+ cells (total number counted in black) that are also positive for C1q (% in green). Scale bar: 50 μm.

(C) Immunofluorescence to detect Pax7 and MHC-II on sections from non-injured and 5, 10 and 21 DPI TA muscle. Left panel: MHCII single channel, right panel: merged. Bar on right: quantification of Pax7+ cells (total number counted in black) also positive for MHC II (% in green). Scale bar: 50 μm.

(D) Images MuSCs isolated 5 DPI from Pax7CreER:sfGFP mice using FACS based on nuclear-membrane GFP (top) and MHCII (middle). The merged panels (bottom) highlight the surface localization of MHCII expression in Pax7-progeny cells (related to Figures S12A and S12B).

(E) Plot to highlight the potential interactions of immunomyoblasts with all other cells. Interactions are primarily enriched from IMB to DCs, FAPs, and monocytes. Abbreviations: APC, antigen-presenting cells; CTX, cardiotoxin; DCs, dendritic cells; Dividing IC, dividing immune cells; DPI, days post injury; ECs, endothelial cells; FAPs, fibro-adipogenic progenitors; MΦ, macrophages; MuSCs, muscle satellite cells; TA, tibialis anterior muscle.

showed increased expression of these markers (Figure 5A). Specifically, *Ctsb*, *C1qa*, *Ctqc*, and *Lyz2* were not detectable in MuSCs isolated from non-injured muscles but were expressed in MuSCs isolated from 5 DPI muscles. As mRNA does not always correlate to protein expression (Liu et al., 2016), we performed immunofluorescence (IF) with selected antibodies on muscle sections or myoblasts growing on cultured

myofibers. We first probed the expression of C1q and Pax7 by IF from non-injured and 5, 10, and 21 DPI samples. Quantification of C1q and Pax7 co-expression suggested that only a subset of Pax7-positive cells was also positive for C1q and this was dynamic during the course of regeneration, corroborating the results from our scRNA-seq dataset (Figure 5B). Co-localization of Pax7 and C1q was highest at 10 DPI (61% of Pax7+ cells were also C1q$^+$) and subsequently decreased by 21 DPI to 20% (Figure 5B). Since MHC II expression was also enriched in the *in silico* identified immunomyoblast subpopulation, we evaluated the co-expression of Pax7 and MHC II on muscle sections from non-injured and 5, 10 and 21 DPI (Figure 5C). Quantification of Pax7 and MHC II co-localization confirmed that a subset of Pax7$^+$ cells are also positive for MHC II, and the co-expression of Pax7 and MHC II is enriched at 10 DPI (17%, Figure 5C). Given that MHC II is a surface protein primarily expressed in antigen-presenting cells (Rock et al., 2016), we used FACS and the *Pax7^{CreER}:sfGFP* reporter mouse to better resolve MHC II expression in MuSCs. We digested hindlimb muscle from 5 DPI mice, stained with MHC II conjugated to PE or the respective isotype control, and subjected the samples to FACS to determine the presence of any GFP$^+$/MHC II$^+$ cells. Only a subset of GFP$^+$ cells were also MHC II positive after injury, whereas the isotype control did not exhibit binding, suggesting that the MHC II antibody is specific for the target antigen (Figure S12B). Furthermore, imaging of 5 DPI MuSCs after FACS clearly demonstrated surface expression of MHC II (Figure 5D). Finally, we evaluated the expression of Ctsb and Apoe by IF using single myofiber culture, as this is commonly used to mimic the MuSC-myofiber interaction *in vitro* (Bischoff, 1986). Indeed, a subset of Myod$^+$ cells were also positive for cytoplasmic Ctsb (28%, Figure S12C), whereas ApoE was detected in the cytoplasm 22% of Myod$^+$ cells (Figure S12D). Overall, these data suggest that a subpopulation of MuSCs enriched in immune-gene expression may transiently exist after muscle injury, consistent with the identification of this population *in silico* in our scRNA-seq data.

To further explore the potential function of this subpopulation, we analyzed enrichment of receptor-ligand pairs between immunomyoblasts and all other meta-clusters (from Figure 1B). Given that immunomyoblasts were enriched for immune-related genes, it was not surprising that receptor-ligand pairs were also enriched between immunomyoblasts and immune cell populations (Figures 5E and Table S5). Although the functional impact of this subpopulation remains to be determined, our data suggest that MuSCs can activate an immunogenic transcriptional program that may play a role in muscle regeneration and/or immune cell modulation in response to injury.

DISCUSSION

Our data containing the transcripts of over 53,000 cells during muscle regeneration highlights the complex nature of tissue regeneration and identifies a subpopulation of MuSCs with immune gene characteristics. Although batch effects remain a technical and analytic challenge for the present dataset, non-linear batch correction methods aim to minimize the differences observed across similar samples processed using different platforms or under different experimental conditions (Stuart et al., 2019). Given that each sample in our dataset is a unique time point, we did not perform batch correction as we did not have multiple samples from the same time point (although samples were processed as uniformly as possible). Therefore, our datasets were merged and subsequently analyzed in order to preserve the expected heterogeneity across regeneration time points. PCA and UMAP embedding highlight that samples cluster by regeneration time point and not by batch (Figure S3). However, future experiments to include cell tagging will clarify potential batch effects across regeneration time points (Gehring et al., 2020; Kong et al., 2020). Nonetheless, our dataset recapitulates key features of muscle regeneration. Specifically, the immune cell populations were the largest in number and displayed the most time-dependent dynamics. Although 21 DPI immune characteristics approached the non-injured muscle state, they were fairly distinct as we detected small populations of pro- and anti-inflammatory populations, dendritic cells, T cells, and leukocytes. These late-regeneration-stage immune cells may function to further model the regenerated muscle or may be a signature of injured muscle and thereby impart a "memory" on the injured muscle (Burzyn et al., 2013), which will be important to consider for clinical applications in which injury precedes therapy.

In contrast to the immediate and subsequent resolution of the immune response, the mesenchymal populations displayed a linear trajectory from activated FAPs through to the non-injured subpopulations. In non-injured muscle, we identified two subpopulations of FAPs. One, which we termed Cxcl14$^+$ FAPs, and another Dpp4$^+$ population with similar features to the reticular interstitial progenitors identified in mouse and human adipose tissue and recently described in muscle (Merrick et al., 2019; Scott et al., 2019). Upon injury, activated FAPs were transcriptionally distinct from the non-injured populations and

progressed to Wisp1$^+$ FAPs at 3.5 and 5 DPI. The transient expression of *Wisp1* in the FAP population was consistent with a recently reported function for Wisp1 in FAPs, in which its expression is enriched in FAPs at 3 DPI and required for MuSC asymmetric expansion (Lukjanenko et al., 2019). Thus, this population of FAPs warrants further investigation as they may play a role in MuSC function and skeletal muscle regeneration as a whole. Our dataset also identified a subpopulation of Dlk1$^+$ FAPs that appeared to be specific to 10 DPI. Interestingly, Dlk1 is a marker for pre-adipocytes and FAP accumulation can lead to intra-muscular adipocyte infiltration (Biferali et al., 2019; Hudak and Sul, 2013). Whether the Dlk1+ FAP population represents a pre-adipocyte state during muscle regeneration will also require future studies. At 21 DPI, we detected a unique population of fibroblasts enriched for collagen type 1 gene expression and therefore may represent persistent, unresolved fibrosis after injury. Osr1$^+$ FAPs were the predominant cell type present at 21 DPI, and a small population of Osr1$^+$ FAPs was also present in non-injured muscle. A recent report suggests that Osr1$^+$ FAPs constitute the FAP progenitor pool in response to freeze injury (Stumm et al., 2018). However, our data did not imply any specific progenitor population and, more strikingly, did not identify a subset of FAPs enriched for cell-cycle-related genes. These data demonstrate the possibly diverse role of the FAP populations and will serve as a platform to further our understanding of the functional significance of these subpopulations.

The striking dynamics of the immune and mesenchymal populations prompted us to further explore MuSC transcriptional features, by which we identified a subpopulation of MuSCs enriched for immune-related genes. We determined by IF that a subpopulation of MuSCs indeed express immune-related genes upon injury and further evaluated the expression of MHC II on the surface of a subset of MuSCs via FACS. This subpopulation of MuSCs has not been defined as a discrete subpopulation but overlaps with the previously described literature. Early studies suggested that a specific subset of bone-marrow-derived stem cells contribute to muscle regeneration through fusion into the newly regenerated myofibers and that Cd45$^+$ cells can be myogenic upon muscle injury (Doyonnas et al., 2004; Palermo et al., 2005; Polesskaya et al., 2003; Seale et al., 2004). MuSCs can also act as antigen-presenting cells upon viral transduction (Cao et al., 2004), suggesting an immune transcriptional program exists in MuSCs. A recent study further suggests that non-hematopoietic cells can express MHC II (Wosen et al., 2018). Various datasets analyzing the expression profiles of quiescent and activated MuSCs also show that inflammatory gene signatures are enriched in activated MuSCs (Pietrosemoli et al., 2017). However, these studies used bulk-RNA methods and thus were unable to assign the expression of inflammatory and complement-related transcripts to a specific subpopulation. Furthermore, a recent study identified immune-related gene expression networks by RNA-sequencing of Pax3-positive cells in mouse limb during fetal myogenesis (Singh et al., 2018), when a subset of embryonic myoblasts take the sublaminar position to become MuSCs. Similarly, our *in silico* analysis showed that IMBs were most abundant at 21 DPI, perhaps suggesting a synergism between the immune system and the homing of quiescent MuSCs upon completion of regeneration. Interestingly, at 21 DPI we detected a diverse range of immune cells including pro-inflammatory subsets, which may secret pro-inflammatory cytokines to promote the expansion of MuSCs including IMBs (Fu et al., 2015). Although further functional analyses will be required to confirm if the IMBs represent a true subpopulation of MuSCs with a specific function, our single cell transcriptional profiling and preliminary IF and FACS data provide evidence for the existence of this subpopulation of transitional myoblasts.

Limitations of the Study

Given that each time point was a single sample, there may be batch effects that cannot be teased out with the current dataset. Although PCA, clustering, and UMAP embedding did not suggest a strong batch effect, future experiments to include cell tagging or additional samples will be necessary to elucidate batch effects. *In silico* identification of a subpopulation of MuSCs enriched for immune-gene expression (immunomyoblasts) will require further functional validation to confirm that this subpopulation is not an artifact of scRNA-seq sample preparation. Although IF suggested that a subset of MuSCs express C1q and MHC-II upon muscle injury, future efforts to evaluate the transcriptional features and functional role of this MuSCs population will help determine the functional relevance of this subpopulation in muscle regeneration.

METHODS

All methods can be found in the accompanying Transparent Methods supplemental file.

AUTHOR CONTRIBUTIONS

S.N.O. conceived and conducted the experiments, performed the data analysis, and wrote the paper; F.Y. helped with experimental design and performed experiments; J.Q. performed experiments; L.F.B. helped with data analysis; S.K. conceived and supervised the project, analyzed the data, and revised the manuscript. All authors read and provided feedback on the manuscript.

DECLARATION OF INTERESTS

The authors declare that they have no conflicts of interest with the contents of this article.

REFERENCES

Arnold, L., Henry, A., Poron, F., Baba-Amer, Y., van Rooijen, N., Plonquet, A., Gherardi, R.K., and Chazaud, B. (2007). Inflammatory monocytes recruited after skeletal muscle injury switch into antiinflammatory macrophages to support myogenesis. J. Exp. Med. 204, 1057–1069.

Baghdadi, M.B., and Tajbakhsh, S. (2018). Regulation and phylogeny of skeletal muscle regeneration. Dev. Biol. 433, 200–209.

Biferali, B., Proietti, D., Mozzetta, C., and Madaro, L. (2019). Fibro–adipogenic progenitors cross-talk in skeletal muscle: the social network. Front. Physiol. 10, 1074.

Bischoff, R. (1986). Proliferation of muscle satellite cells on intact myofibers in culture. Dev. Biol. 115, 129–139.

Boisset, J.-C., Vivié, J., Grün, D., Muraro, M.J., Lyubimova, A., and van Oudenaarden, A. (2018). Mapping the physical network of cellular interactions. Nat. Methods 15, 547–553.

Braza, M.S., Conde, P., Garcia, M., Cortegano, I., Brahmachary, M., Pothula, V., Fay, F., Boros, P., Werner, S.A., Ginhoux, F., et al. (2018). Neutrophil derived CSF1 induces macrophage polarization and promotes transplantation tolerance. Am. J. Transplant. 18, 1247–1255.

Burzyn, D., Kuswanto, W., Kolodin, D., Shadrach, J.L., Cerletti, M., Jang, Y., Sefik, E., Tan, T.G., Wagers, A.J., Benoist, C., et al. (2013). A special population of regulatory T cells potentiates muscle repair. Cell 155, 1282–1295.

Butler, A., Hoffman, P., Smibert, P., Papalexi, E., and Satija, R. (2018). Integrating single-cell transcriptomic data across different conditions, technologies, and species. Nat. Biotechnol. 36, 411–420.

Cao, B., Bruder, J., Kovesdi, I., and Huard, J. (2004). Muscle stem cells can act as antigen-presenting cells: implication for gene therapy. Gene Ther. 11, 1321–1330.

Christov, C., Chrétien, F., Abou-Khalil, R., Bassez, G., Vallet, G., Authier, F.-J., Bassaglia, Y., Shinin, V., Tajbakhsh, S., Chazaud, B., et al. (2007). Muscle satellite cells and endothelial cells: close neighbors and privileged partners. Mol. Biol. Cell 18, 1397–1409.

Cordero-Espinoza, L., and Huch, M. (2018). The balancing act of the liver: tissue regeneration versus fibrosis. J. Clin. Invest. 128, 85–96.

Dell'orso, S., Juan, A.H., Ko, K.-D., Naz, F., Gutierrez-Cruz, G., Feng, X., and Sartorelli, V. (2019). Single-cell analysis of adult skeletal muscle stem cells in homeostatic and regenerative conditions. Development 146, dev174177.

Deng, B., Wehling-Henricks, M., Villalta, S.A., Wang, Y., and Tidball, J.G. (2012). IL-10 triggers changes in macrophage phenotype that promote muscle growth and regeneration. J. Immunol. 189, 3669–3680.

Doyonnas, R., LaBarge, M.A., Sacco, A., Charlton, C., and Blau, H.M. (2004). Hematopoietic contribution to skeletal muscle regeneration by myelomonocytic precursors. Proc. Natl. Acad. Sci. U S A 101, 13507–13512.

Fu, X., Xiao, J., Wei, Y., Li, S., Liu, Y., Yin, J., Sun, K., Sun, H., Wang, H., Zhang, Z., et al. (2015). Combination of inflammation-related cytokines promotes long-term muscle stem cell expansion. Cell Res. 25, 655–673.

Fukada, S., Uezumi, A., Ikemoto, M., Masuda, S., Segawa, M., Tanimura, N., Yamamoto, H., Miyagoe-Suzuki, Y., and Takeda, S. (2007). Molecular signature of quiescent satellite cells in adult skeletal muscle. Stem Cells 25, 2448–2459.

Garry, G.A., Antony, M.L., and Garry, D.J. (2016). Cardiotoxin induced injury and skeletal muscle regeneration. In Methods in Molecular Biology, N.J. Clifton, ed. (Humana Press, Inc.), pp. 61–71.

Gehring, J., Hwee Park, J., Chen, S., Thomson, M., and Pachter, L. (2020). Highly multiplexed single-cell RNA-seq by DNA oligonucleotide tagging of cellular proteins. Nat. Biotechnol. *38*, 35–38.

Gerber, T., Gerber, T., Murawala, P., Knapp, D., Masselink, W., Schuez, M., Gac-santel, M., Nowoshilow, S., Kageyama, J., Khattak, S., et al. (2018). Single-cell analysis uncovers convergence of cell identities during axolotl limb regeneration. Science *362*, https://doi.org/10.1126/science.aaq0681.

Giordani, L., He, G.J., Negroni, E., Sakai, H., Law, J.Y.C., Siu, M.M., Wan, R., Corneau, A., Tajbakhsh, S., Cheung, T.H., et al. (2019). High-Dimensional single-cell cartography reveals novel skeletal muscle-resident cell populations. Mol. Cell *74*, 609–621.e6.

Goodyear, A.W., Kumar, A., Dow, S., and Ryan, E.P. (2014). Optimization of murine small intestine leukocyte isolation for global immune phenotype analysis. J. Immunol. Methods *405*, 97–108.

Halpern, K.B., Shenhav, R., Massalha, H., Toth, B., Egozi, A., Massasa, E.E., Medgalia, C., David, E., Giladi, A., Moor, A.E., et al. (2018). Paired-cell sequencing enables spatial gene expression mapping of liver endothelial cells. Nat. Biotechnol. *36*, 962.

Hardy, D., Besnard, A., Latil, M., Jouvion, G., Briand, D., Thépenier, C., Pascal, Q., Guguin, A., Gayraud-Morel, B., Cavaillon, J.-M., et al. (2016). Comparative study of injury models for studying muscle regeneration in mice. PLoS One *11*, e0147198.

Heredia, J.E., Mukundan, L., Chen, F.M., Mueller, A.A., Deo, R.C., Locksley, R.M., Rando, T.A., and Chawla, A. (2013). Type 2 innate signals stimulate fibro/adipogenic progenitors to facilitate muscle regeneration. Cell *153*, 376–388.

Hudak, C.S., and Sul, H.S. (2013). Pref-1, a gatekeeper of adipogenesis. Front. Endocrinol. (Lausanne) *4*, 79.

Hwang, B., Lee, J.H., and Bang, D. (2018). Single-cell RNA sequencing technologies and bioinformatics pipelines. Exp. Mol. Med. *50*, 96.

Joe, A.W.B., Yi, L., Natarajan, A., Le Grand, F., So, L., Wang, J., Rudnicki, M.A., and Rossi, F.M.V. (2010). Muscle injury activates resident fibro/adipogenic progenitors that facilitate myogenesis. Nat. Cell Biol. *12*, 153–163.

Juhas, M., Abutaleb, N., Wang, J.T., Ye, J., Shaikh, Z., Sriworarat, C., Qian, Y., and Bursac, N. (2018). Incorporation of macrophages into engineered skeletal muscle enables enhanced muscle regeneration. Nat. Biomed. Eng. *2*, 942–954.

Kong, W., Biddy, B.A., Kamimoto, K., Amrute, J.M., Butka, E.G., and Morris, S.A. (2020). CellTagging: combinatorial indexing to simultaneously map lineage and identity at single-cell resolution. Nat. Protoc. *15*, 1–23.

Kumar, M.P., Du, J., Lagoudas, G., Jiao, Y., Sawyer, A., Drummond, D.C., Lauffenburger, D.A., and Raue, A. (2018). Analysis of single-cell RNA-seq identifies cell-cell communication associated with tumor characteristics. Cell Rep. *25*, 1458–1468.e4.

Lagha, M., Mayeuf-Louchart, A., Chang, T., Montarras, D., Rocancourt, D., Zalc, A., Kormish, J., Zaret, K.S., Buckingham, M.E., and Relaix, F. (2013). Itm2a is a Pax3 target gene, expressed at sites of skeletal muscle formation in vivo. PLoS One *8*, e63143.

Larouche, J., Greising, S.M., Corona, B.T., and Aguilar, C.A. (2018). Robust inflammatory and fibrotic signaling following volumetric muscle loss: a barrier to muscle regeneration. Cell Death Dis. *9*, 409.

Latroche, C., Weiss-Gayet, M., Muller, L., Gitiaux, C., Leblanc, P., Liot, S., Ben-Larbi, S., Abou-Khalil, R., Verger, N., Bardot, P., et al. (2017). Coupling between myogenesis and angiogenesis during skeletal muscle regeneration is stimulated by restorative macrophages. Stem Cell Reports *9*, 2018–2033.

Liu, Y., Beyer, A., and Aebersold, R. (2016). On the dependency of cellular protein levels on mRNA abundance. Cell *165*, 535–550.

Lu, H., Huang, D., Ransohoff, R.M., and Zhou, L. (2011). Acute skeletal muscle injury: CCL2 expression by both monocytes and injured muscle is required for repair. FASEB J. *25*, 3344–3355.

Lukjanenko, L., Karaz, S., Stuelsatz, P., Gurriaran-Rodriguez, U., Michaud, J., Dammone, G., Sizzano, F., Mashinchian, O., Ancel, S., Migliavacca, E., et al. (2019). Aging disrupts muscle stem cell function by impairing matricellular WISP1 secretion from fibro-adipogenic progenitors. Cell Stem Cell *24*, 433–446.e7.

Luo, C., Keown, C.L., Kurihara, L., Zhou, J., He, Y., Li, J., Castanon, R., Lucero, J., Nery, J.R., Sandoval, J.P., et al. (2017). Single-cell methylomes identify neuronal subtypes and regulatory elements in mammalian cortex. Science *357*, 600–604.

Malecova, B., Gatto, S., Etxaniz, U., Passafaro, M., Cortez, A., Nicoletti, C., Giordani, L., Torcinaro, A., De Bardi, M., Bicciato, S., et al. (2018). Dynamics of cellular states of fibro-adipogenic progenitors during myogenesis and muscular dystrophy. Nat. Commun. *9*, 3670.

Merrick, D., Sakers, A., Irgebay, Z., Okada, C., Calvert, C., Morley, M.P., Percec, I., and Seale, P. (2019). Identification of a mesenchymal progenitor cell hierarchy in adipose tissue. Science *364*, eaav2501.

Micheli, A.J. De, Fraczek, P., Soueid-Baumgarten, S., Ravichandran, H., Vlaminck, I. De, Elemento, O., and Cosgrove, B.D. (2019). Single-cell analysis of the muscle stem cell hierarchy identifies heterotypic communication signals involved in skeletal muscle regeneration. bioRxiv, 671032.

Moyer, A.L., and Wagner, K.R. (2011). Regeneration versus fibrosis in skeletal muscle. Curr. Opin. Rheumatol. *23*, 568–573.

Murphy, M.M., Lawson, J.A., Mathew, S.J., Hutcheson, D.A., and Kardon, G. (2011). Satellite cells, connective tissue fibroblasts and their interactions are crucial for muscle regeneration. Development *138*, 3625–3637.

Palermo, A.T., LaBarge, M.A., Doyonnas, R., Pomerantz, J., and Blau, H.M. (2005). Bone marrow contribution to skeletal muscle: a physiological response to stress. Dev. Biol. *279*, 336–344.

Pawlikowski, B., Betta, N.D., Elston, T., O'Rourke, R., Jones, K., and Olwin, B.B. (2019). A cellular atlas of skeletal muscle regeneration and aging. bioRxiv, 635805.

Paylor, B., Natarajan, A., Zhang, R.-H., and Rossi, F. (2011). Nonmyogenic cells in skeletal muscle regeneration. Curr. Top. Dev. Biol. *96*, 139–165.

Pietrosemoli, N., Mella, S., Yennek, S., Baghdadi, M.B., Sakai, H., Sambasivan, R., Pala, F., Di Girolamo, D., and Tajbakhsh, S. (2017). Comparison of multiple transcriptomes exposes unified and divergent features of quiescent and activated skeletal muscle stem cells. Skelet. Muscle *7*, 28.

Polesskaya, A., Seale, P., and Rudnicki, M.A. (2003). Wnt signaling induces the myogenic specification of resident CD45+ adult stem cells during muscle regeneration. Cell *113*, 841–852.

Ramilowski, J.A., Goldberg, T., Harshbarger, J., Kloppmann, E., Lizio, M., Satagopam, V.P., Itoh, M., Kawaji, H., Carninci, P., Rost, B., et al. (2015). A draft network of ligand–receptor-mediated multicellular signalling in human. Nat. Commun. *6*, 7866.

Relaix, F., and Zammit, P.S. (2012). Satellite cells are essential for skeletal muscle regeneration: the cell on the edge returns centre stage. Development *139*, 2845–2856.

Rock, K.L., Reits, E., and Neefjes, J. (2016). Present yourself! By MHC class I and MHC class II molecules. Trends Immunol. *37*, 724–737.

Saelens, W., Cannoodt, R., Todorov, H., and Saeys, Y. (2019). A comparison of single-cell trajectory inference methods. Nat. Biotechnol. *37*, 547–554.

Seale, P., Ishibashi, J., Scimè, A., and Rudnicki, M.A. (2004). Pax7 is necessary and sufficient for the myogenic specification of CD45+:sca1+ stem cells from injured muscle. PLoS Biol. *2*, e130.

Segawa, M., Fukada, S., Yamamoto, Y., Yahagi, H., Kanematsu, M., Sato, M., Ito, T., Uezumi, A., Hayashi, S., Miyagoe-Suzuki, Y., et al. (2008). Suppression of macrophage functions impairs skeletal muscle regeneration with severe fibrosis. Exp. Cell Res. *314*, 3232–3244.

Shea, K.L., Xiang, W., LaPorta, V.S., Licht, J.D., Keller, C., Basson, M.A., and Brack, A.S. (2010). Sprouty1 regulates reversible quiescence of a self-renewing adult muscle stem cell pool during regeneration. Cell Stem Cell *6*, 117–129.

Singh, A.J., Chang, C.-N., Ma, H.-Y., Ramsey, S.A., Filtz, T.M., and Kioussi, C. (2018). FACS-Seq analysis of Pax3-derived cells identifies non-myogenic lineages in the embryonic forelimb. Sci. Rep. *8*, 7670.

Scott, R.W., Arostegui, M., Schweitzer, R., Rossi, F.M., and Underhill, T.M. (2019). Hic1 defines quiescent mesenchymal progenitor subpopulations with distinct functions and fates in skeletal muscle regeneration. Cell Stem Cell *25*, 797–813.e9.

Street, K., Risso, D., Fletcher, R.B., Das, D., Ngai, J., Yosef, N., Purdom, E., and Dudoit, S. (2018). Slingshot: cell lineage and pseudotime inference for single-cell transcriptomics. BMC Genomics 19, 477.

Stuart, T., Butler, A., Hoffman, P., Stoeckius, M., Smibert, P., Satija, R., Hafemeister, C., Papalexi, E., Mauck, W.M., III, and Hao, Y. (2019). Comprehensive integration of single-cell data resource comprehensive integration of single-cell data. Cell 177, 1888–1902.e21.

Stumm, J., Vallecillo-García, P., Vom Hofe-Schneider, S., Ollitrault, D., Schrewe, H., Economides, A.N., Marazzi, G., Sassoon, D.A., and Stricker, S. (2018). Odd skipped-related 1 (Osr1) identifies muscle-interstitial fibro-adipogenic progenitors (FAPs) activated by acute injury. Stem Cell Res. 32, 8–16.

Subramanian, A., and Schilling, T.F. (2015). Tendon development and musculoskeletal assembly: emerging roles for the extracellular matrix. Development 142, 4191–4204.

Tidball, J.G., and Wehling-Henricks, M. (2007). Macrophages promote muscle membrane repair and muscle fibre growth and regeneration during modified muscle loading in mice in vivo. J. Physiol. 578, 327–336.

Trapecar, M., Khan, S., Roan, N.R., Chen, T.-H., Telwatte, S., Deswal, M., Pao, M., Somsouk, M., Deeks, S.G., Hunt, P.W., et al. (2017). An optimized and validated method for isolation and characterization of lymphocytes from HIV+ human gut biopsies. AIDS Res. Hum. Retroviruses 33, S31–S39.

Trapnell, C., Cacchiarelli, D., Grimsby, J., Pokharel, P., Li, S., Morse, M., Lennon, N.J., Livak, K.J., Mikkelsen, T.S., and Rinn, J.L. (2014). The dynamics and regulators of cell fate decisions are revealed by pseudotemporal ordering of single cells. Nat. Biotechnol. 32, 381–386.

van Velthoven, C.T.J., de Morree, A., Egner, I.M., Brett, J.O., and Rando, T.A. (2017). Transcriptional profiling of quiescent muscle stem cells in vivo. Cell Rep. 21, 1994–2004.

Villalta, S.A., Rinaldi, C., Deng, B., Liu, G., Fedor, B., and Tidball, J.G. (2011). Interleukin-10 reduces the pathology of mdx muscular dystrophy by deactivating M1 macrophages and modulating macrophage phenotype. Hum. Mol. Genet. 20, 790–805.

Wang, X., Allen, W.E., Wright, M.A., Sylwestrak, E.L., Samusik, N., Vesuna, S., Evans, K., Liu, C., Ramakrishnan, C., Liu, J., et al. (2018). Three-dimensional intact-tissue sequencing of single-cell transcriptional states. Science 361, https://doi.org/10.1126/science.aat5691.

Wosen, J.E., Mukhopadhyay, D., MacAubas, C., and Mellins, E.D. (2018). Epithelial MHC class II expression and its role in antigen presentation in the gastrointestinal and respiratory tracts. Front. Immunol. 9, 2144.

Wynn, T.A., and Vannella, K.M. (2016). Macrophages in tissue repair, regeneration, and fibrosis. Immunity 44, 450–462.

Yang, W., and Hu, P. (2018). Skeletal muscle regeneration is modulated by inflammation. J. Orthop. Transl. 13, 25–32.

Ye, A., He, H., and Kim, J. (2014). Paternally expressed Peg3 controls maternally expressed Zim1 as a trans factor. PLoS One 9, e108596.

Yin, H., Price, F., and Rudnicki, M.A. (2013). Satellite cells and the muscle stem cell niche. Physiol. Rev. 93, 23–67.

Yue, F., Bi, P., Wang, C., Shan, T., Nie, Y., Ratliff, T.L., Gavin, T.P., and Kuang, S. (2017). Pten is necessary for the quiescence and maintenance of adult muscle stem cells. Nat. Commun. 8, 14328.

Zeng, T., and Dai, H. (2019). Single-cell RNA sequencing-based computational analysis to describe disease heterogeneity. Front. Genet. 10, 629.

Zilionis, R., Engblom, C., Pfirschke, C., Savova, V., Zemmour, D., Saatcioglu, H.D., Krishnan, I., Maroni, G., Meyerovitz, C.V., Kerwin, C.M., et al. (2019). Single-cell transcriptomics of human and mouse lung cancers reveals conserved myeloid populations across individuals and species. Immunity 50, 1317–1334.e10.

Supplemental Information

Temporal Dynamics and Heterogeneity

of Cell Populations

during Skeletal Muscle Regeneration

Stephanie N. Oprescu, Feng Yue, Jiamin Qiu, Luiz F. Brito, and Shihuan Kuang

Cell meta-clusters	0.5 DPI	2 DPI	3.5 DPI	5 DPI	10 DPI	21 DPI	Non-inj
FAPs	339	447	1294	2105	2241	4135	3492
Myonuclei	5	9	3	1	139	304	1368
MuSC	9	26	424	536	301	255	176
Endothelial cells	6	25	34	97	120	301	43
Monocytes	1552	1946	1604	555	255	413	61
APC	186	505	834	767	393	335	73
Tcells	45	54	291	310	225	85	136
Tenocytes	0	4	16	66	227	555	132
M2 Macrophage	0	55	5878	4229	2018	483	31
Neutrophils	1311	2143	87	68	27	130	115
ProliferatingIC	0	56	365	243	24	21	6
Pericytes	1	5	3	29	55	245	14
Myeloid cells	5	33	342	338	94	56	16
M1 Macrophage	51	3080	66	124	3	45	3
Fibroblasts	0	7	10	23	92	1299	4

Table S1. Cell counts per sample; related to Figure 1. Cell counts for each sample.

Cxcl14 FAPs	Dpp4 FAPs	Dlk1 FAPs	Osr1 FAPs	Wisp1 FAPs	Activated FAPs	Fibroblasts
Cxcl14	Pi16	Dlk1	Gsn	Postn	Cxcl5	Meg3
Smoc2	Igfbp5	Itm2a	Mgp	Csrp2	Prg4	Col3a1
Ccl11	Igfbp6	Meg3	Dcn	Sfrp2	Timp1	Dlk1
Gsn	Fbn1	Igf2	Smoc2	Ptn	Mt2	Itm2a
Dcn	Ugdh	Cdkn1c	Col3a1	Cthrc1	Cxcl1	Col1a1
Hsd11b1	Cd55	Col3a1	Egr1	H19	Ptx3	Col1a2
Crispld2	Pcolce2	H19	Apod	Tnc	Mmp3	Gnas
Col4a1	Ly6c1	Mfap4	Cxcl14	Col8a1	Ccl2	Sparc
Lum	Mfap5	Mest	Myoc	Lox	Tnfaip6	Col6a3
Dpep1	Efemp1	Plagl1	Lum	Mest	Pdpn	Lum
Apod	Clec3b	Col1a1	Col4a1	Acta2	Ccl7	Col5a2
Rarres2	Myoc	Postn	Serping1	Ccdc80	Serpine1	Postn
Htra3	Cd34	Lum	Col15a1	Col12a1	Uap1	Aspn
Itih5	Adamts5	Peg3	Sparcl1	Thbs2	Tnc	Mfap5
Col15a1	Sema3c	Mfap2	Itih5	Serpine1	Il33	Col6a2
Col4a2	Has1	Col6a3	Abca8a	Sfrp1	Cxcl14	Igfbp4
Clec3b	Fstl1	Col1a2	Clec3b	Cilp	Tm4sf1	Fstl1
Myoc	Pcsk6	Mfap5	Serpinf1	Timp1	Fst	Mgp
Hspg2	Gfpt2	Cilp	Nid1	Maged1	Mt1	Col6a1
Abca8a	Plpp3	Col14a1	Lpl	Tm4sf1	Il1rl1	Bgn
Serping1	Gsn	Col5a2	Col4a2	Dpysl3	Thbd	Col5a1
Col5a3	Ackr3	Col6a2	Sparc	1500015O10Rik	Ncl	Pcolce
Egr1	Cd248	Aspn	Htra3	Prrx1	Rdh10	Dpt
Lama2	Anxa3	Mgp	Mmp2	Rcn1	Has1	Ccdc80
Fos	Ly6a	Col6a1	Igfbp7	Angptl4	Cald1	Ppic
Tnxb	C3	Sparc	Hspa1b	Loxl1	Aldh1a2	Nid1
Plxdc2	Uap1	Igfbp4	Zbtb20	Cxcl12	Inhba	Ebf1
Serpinf1	Tnxb	Gnas	Dpep1	Col16a1	Il6	Aebp1
Gstm1	Dpt	Fstl1	Col6a2	Mxra8	Adamts1	Rcn3
Ier2	Klf4	Islr	Ccl11	Grb10	Ugdh	Nfib
Jund	Nid1	Pcolce	Cygb	Maged2	Lox	Itih5
Col6a2	Pla1a	Nrep	Col6a1	Tagln	Npm1	Mmp2
Lamc1	Procr	Col5a1	Ltbp4	Fkbp10	Ran	Col5a3
Enpp2	Rarres2	Bgn	Gas1	Efemp2	Srm	Serping1
Col6a1	Serping1	Nid1	Col5a3	Rbp1	Cxcl12	Cyr61
Adamts5	Lrrn4cl	Ptn	Col6a3	Srpx2	Gfpt2	Mt2
Cyb5a	Tnfaip6	Itih5	Nfib	Dclk1	Fbln2	Col4a1
Pcolce	Timp3	Maged2	Col1a2	Ptx3	Nop58	Fbn1
Plpp3	Tmem100	Lamb1	Entpd2	Mfap2	Col8a1	Col4a2
Vwa1	Scara5	Dnajb1	Pcolce	Fkbp9	Plau	Ogn
Rnase4	Mt2	Dpt	Igfbp6	Ctgf	Sod3	Clec3b
Podn	Fndc1	Serpinh1	Nfia	Wisp1	Il1r1	Gadd45g
F3	Efhd1	Fbln7	Fos	Emilin1	Eif5a	Cdkn1c
Nid1	Gstm1	Igfbp7	Ogn	C1qtnf6	Tnfrsf12a	Igfbp7
Sdc2	Col14a1	Eln	Pdgfra	Fkbp11	Csf1	Igf2
Abca8b	Ebf1	Swt1	Ebf1	Col14a1	Ybx3	Bag3
Angptl1	Fn1	Kcnq1ot1	Hmcn2	Lrrc15	Angptl4	Fn1
Fbln2	Ecm1	Ccdc80	Adamts5	Mmp23	Csgalnact1	Egr1
Cd34	Ace	Fndc1	Angptl1	Kdelr3	Gnl3	Loxl1
G0s2	Dpp4	Nrk	Cd34	Mfap4	Eef1g	Serpinh1

Table S2. FAP gene signature list; related to Figure 3. List of top 50 gene signatures for each FAP cluster. Determined by using FindAllMarkers() against the entire dataset and thus are genes enriched in the respective FAP sub-population. Abbreviations: FAPs; fibro-adipogenic progenitors.

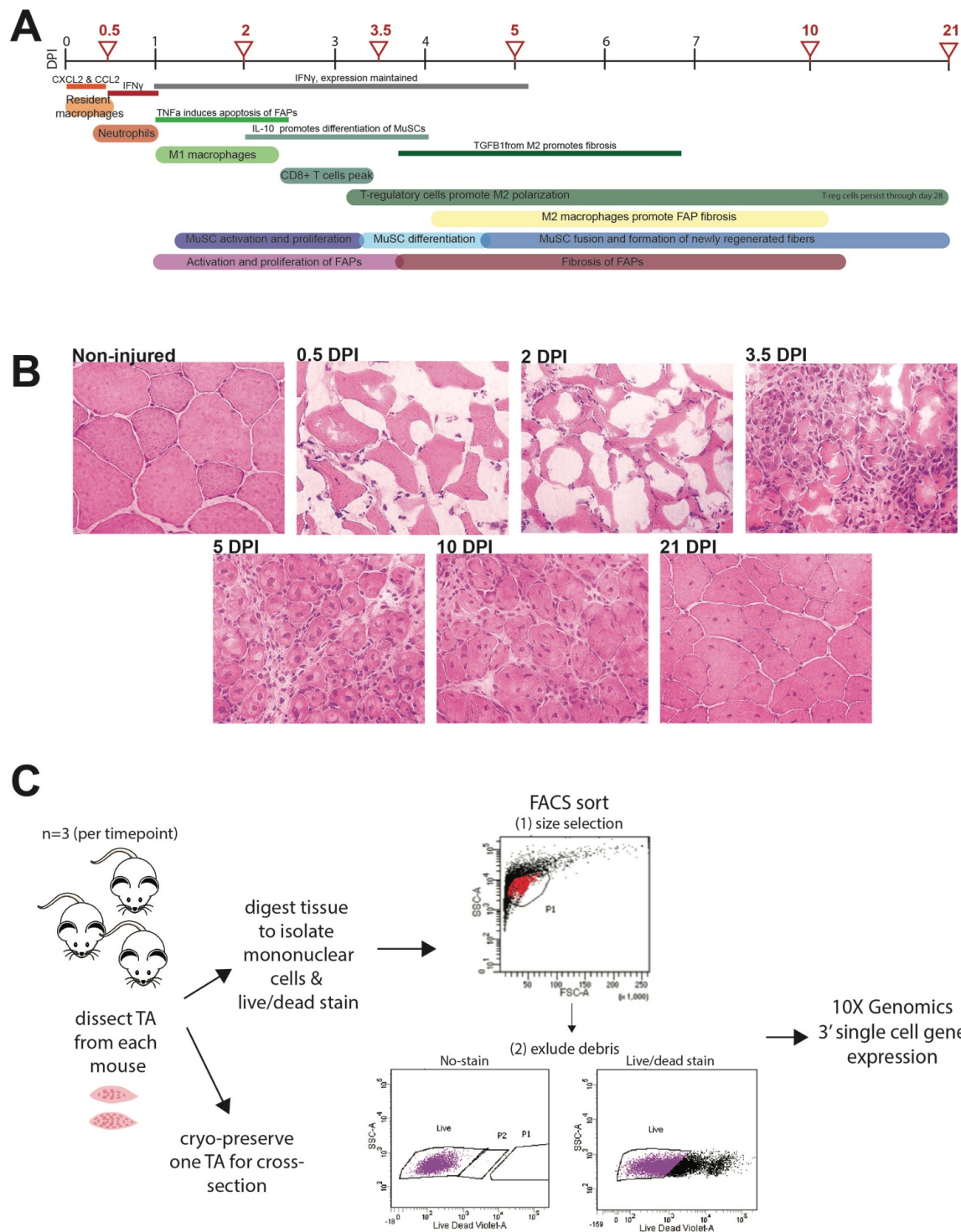| Receptor	Ligand	Cell to	Cell from	Time-point	Receptor	Ligand	Cell to	Cell from	Time-point
MYOC	ALDOA	Dpp4_FAPs	SM	NJ	CCL2	VCAN	ActivatedFAPs	Leukocytes	0.5 DPI
ALDOA	MYOC	SM	Dpp4_FAPs	NJ	VCAN	CCL2	Leukocytes	ActivatedFAPs	0.5 DPI
MYOC	ALDOA	Dpp4_FAPs	SM	21 DPI	CCL2	VCAN	ActivatedFAPs	Leukocytes	2 DPI
ALDOA	MYOC	SM	Dpp4_FAPs	21 DPI	VCAN	CCL2	Leukocytes	ActivatedFAPs	2 DPI
ALDOA	CRISPLD2	SM	Cxcl14_FAPs	NJ	THBS1	DCN	Leukocytes	Osr1_FAPs	21 DPI
CRISPLD2	ALDOA	Cxcl14_FAPs	SM	NJ	CCRL2	CCL7	Neutrophils	ActivatedFAPs	0.5 DPI
TIMP1	TNF	ActivatedFAPs	Neutrophils	0.5 DPI	CCRL2	CCL7	Neutrophils	ActivatedFAPs	2 DPI
TIMP1	TNF	ActivatedFAPs	Neutrophils	2 DPI	COL1A1	DCN	Tenocytes	Cxcl14_FAPs	NJ
CXCL1	TNF	ActivatedFAPs	Neutrophils	0.5 DPI	DCN	COL1A1	Cxcl14_FAPs	Tenocytes	NJ
CXCL1	TNF	ActivatedFAPs	Neutrophils	2 DPI	VCAN	FBN1	Leukocytes	Dpp4_FAPs	21 DPI
THBS1	IGFBP5	Leukocytes	Dpp4_FAPs	21 DPI	FBN1	VCAN	Dpp4_FAPs	Leukocytes	21 DPI
IGFBP5	THBS1	Dpp4_FAPs	Leukocytes	21 DPI	CCL2	IL1B	ActivatedFAPs	Neutrophils	0.5 DPI
MYOC	ALDOA	Cxcl14_FAPs	SM	NJ	CCL2	IL1B	ActivatedFAPs	Neutrophils	2 DPI
ALDOA	MYOC	SM	Cxcl14_FAPs	NJ	COL1A1	BGN	Tenocytes	Wisp1_FAPs	10 DPI
ALDOA	HSPG2	SM	Cxcl14_FAPs	NJ	GSN	CST3	Osr1_FAPs	Myeloblasts	10 DPI
HSPG2	ALDOA	Cxcl14_FAPs	SM	NJ	CST3	GSN	Myeloblasts	Osr1_FAPs	10 DPI
MYOC	ALDOA	Osr1_FAPs	SM	NJ	THBS1	COL3A1	Leukocytes	Osr1_FAPs	21 DPI
ALDOA	MYOC	SM	Osr1_FAPs	NJ	COL3A1	THBS1	Osr1_FAPs	Leukocytes	21 DPI
MYOC	ALDOA	Osr1_FAPs	SM	10 DPI	DCN	COL11A1	Cxcl14_FAPs	Tenocytes	NJ
ALDOA	MYOC	SM	Osr1_FAPs	10 DPI	PROCR	TNF	Dpp4_FAPs	Neutrophils	NJ
MYOC	ALDOA	Osr1_FAPs	SM	21 DPI	PROCR	TNF	Dpp4_FAPs	Neutrophils	21 DPI
ALDOA	MYOC	SM	Osr1_FAPs	21 DPI	DCN	COL12A1	Cxcl14_FAPs	Tenocytes	NJ
CCL2	TNF	ActivatedFAPs	Neutrophils	0.5 DPI	CD55	IL1B	Dpp4_FAPs	Leukocytes	21 DPI
CCL2	TNF	ActivatedFAPs	Neutrophils	2 DPI	BGN	CD14	Wisp1_FAPs	Neutrophils	2.5 DPI
CCL11	TNF	Cxcl14_FAPs	Neutrophils	NJ	COL1A1	PCOLCE2	Tenocytes	Dpp4_FAPs	NJ
CCRL2	CCL2	Neutrophils	ActivatedFAPs	0.5 DPI	COL1A1	PCOLCE2	Tenocytes	Dpp4_FAPs	21 DPI
CCRL2	CCL2	Neutrophils	ActivatedFAPs	2 DPI	GSN	APOE	Osr1_FAPs	M2	10 DPI
DCN	TNF	Cxcl14_FAPs	Neutrophils	NJ	APOE	GSN	M2	Osr1_FAPs	10 DPI
TNF	DCN	Neutrophils	Cxcl14_FAPs	NJ	PF4	THBD	M1	ActivatedFAPs	2 DPI
CCRL2	CCL11	Neutrophils	Cxcl14_FAPs	NJ	THBD	PF4	ActivatedFAPs	M1	2 DPI
THBS1	FBN1	Leukocytes	Dpp4_FAPs	21 DPI	COL11A1	BGN	Tenocytes	Wisp1_FAPs	10 DPI
BGN	TNF	Wisp1_FAPs	Neutrophils	3.5 DPI	COL1A2	DCN	Tenocytes	Cxcl14_FAPs	NJ
TNF	BGN	Neutrophils	Wisp1_FAPs	3.5 DPI	DCN	COL1A2	Cxcl14_FAPs	Tenocytes	NJ
THBS1	TNFAIP6	Leukocytes	ActivatedFAPs	0.5 DPI	COL12A1	BGN	Tenocytes	Wisp1_FAPs	10 DPI
TNFAIP6	THBS1	ActivatedFAPs	Leukocytes	0.5 DPI	CD14	CD55	Neutrophils	Dpp4_FAPs	NJ
THBS1	TNFAIP6	Leukocytes	ActivatedFAPs	2 DPI	CD55	CD14	Dpp4_FAPs	Neutrophils	NJ
TNFAIP6	THBS1	ActivatedFAPs	Leukocytes	2 DPI	CD14	CD55	Neutrophils	Dpp4_FAPs	21 DPI
CCL7	TNF	ActivatedFAPs	Neutrophils	0.5 DPI	CD55	CD14	Dpp4_FAPs	Neutrophils	21 DPI
CCL7	TNF	ActivatedFAPs	Neutrophils	2 DPI	COL4A1	THBS1	Osr1_FAPs	Leukocytes	21 DPI
SERPINE1	TNF	ActivatedFAPs	Neutrophils	0.5 DPI	THBS1	COL4A1	Leukocytes	Osr1_FAPs	21 DPI
SERPINE1	TNF	ActivatedFAPs	Neutrophils	2 DPI	COL3A1	COL1A1	Dlk1_FAPs	Tenocytes	`0 DPI
DCN	TNF	Osr1_FAPs	Neutrophils	NJ	COL1A2	BGN	Wisp1_FAPs	Wisp1_FAPs	5 DPI
TNF	DCN	Neutrophils	Osr1_FAPs	NJ	COL11A1	PCOLCE2	Tenocytes	Dpp4_FAPs	NJ
DCN	TNF	Osr1_FAPs	Neutrophils	21 DPI	COL11A1	PCOLCE2	Tenocytes	Dpp4_FAPs	21 DPI
TNF	DCN	Neutrophils	Osr1_FAPs	21 DPI	IGFBP7	FBN1	EC	Dpp4_FAPs	21 DPI
CCL2	IL1B	ActivatedFAPs	Leukocytes	0.5 DPI	TNF	IL33	Neutrophils	ActivatedFAPs	0.5 DPI
CCL2	IL1B	ActivatedFAPs	Leukocytes	2 DPI	TNF	IL33	Neutrophils	ActivatedFAPs	2 DPI

Table S3. Select receptor-ligand pairs enriched across FAP sub-populations; related to Figure 3. Time-point indicates which regeneration stage the respective ligand-receptor pairs were enriched.
Abbreviations: FAPs; fibro-adipogenic progenitors, NJ; Non-injured, DPI; days post injury.

IMB gene signatures
Aif1
Lyz2
Apoe
C1qb
Cd74
C1qa
Ctss
Ctsb
Fcer1g
Tyrobp
C1qc
Psap
Ctsd
Cyba
Sepp1
Gm42418
H2-Aa
Ms4a7
Ifi27l2a
H2-Eb1
H2-Ab1
Cst3
Cd52
Grn
Laptm5
Pf4
Gpnmb
B2m
Lgmn
H2-D1
Ftl1
Ctsh
Ifi30
Wfdc17
H2-K1
Trem2
Pltp
Sh3bgrl3
Fabp5
Ms4a6c
Srgn
Cd68
Mpeg1
Mafb
Fxyd5
Ctsc
Ms4a6b
Hexa
Hexb
Slfn2

Table S4. Gene signature list enriched in immunomyoblast population; related to Figure 4. List of top 50 genes enriched in IMB population relative to other MuSC subpopulations.
Abbreviations: MuSC; muscle satellite cells, IMB; immunomyoblasts.

Receptor	Ligand	Cell to	Cell from	Receptor	Ligand	Cell to	Cell from
S100A8	CTSB	Neutrophils	IMB	CST3	APOE	Naïve Tcell	IMB
S100A8	APOE	Neutrophils	IMB	HMGB2	APOE	Cd3 Tcell	IMB
ALDOA	APOE	SM	IMB	GSN	APOE	Dpp4 FAPs	IMB
ALDOA	CTSB	SM	IMB	CTSD	APOE	Ilr7+ Macro	IMB
PTX3	C1QA	ActivatedFAPs	IMB	CTSD	CTSB	Ilr7+ Macro	IMB
PTX3	C1QB	ActivatedFAPs	IMB	SLPI	CTSS	Leukocytes	IMB
GSN	APOE	Cxcl14 FAPs	IMB	SLPI	CTSB	Leukocytes	IMB
DCN	C1QA	Cxcl14 FAPs	IMB	CD74	CD44	IMB	Neutrophils
GSN	APOE	Osr1 FAPs	IMB	CD74	CTSL	IMB	M1
CD74	CTSB	Cd209a DC	IMB	CD74	CTSD	IMB	Ilr7+ Macro
CD74	CTSS	Cd209a DC	IMB	C1QA	DCN	IMB	Cxcl14 FAPs
CST3	CTSS	Myeloblasts	IMB	C1QA	DCN	IMB	Osr1 FAPs
CST3	CTSB	Myeloblasts	IMB	C1QA	PTX3	IMB	ActivatedFAPs
CST3	APOE	Myeloblasts	IMB	C1QA	CTSL	IMB	M1
MYOC	C1QB	Dpp4 FAPs	IMB	CTSS	CST3	IMB	Myeloblasts
HMGB2	APOE	ProliferatingIC	IMB	CTSS	CST3	IMB	Naïve Tcell
APOE	CTSB	M2	IMB	PPT1	APOE	Myeloblasts	IMB
APOE	SERPING1	IMB	Dpp4 FAPs	CTSL	C1QA	M1	IMB
APOE	CST3	IMB	Myeloblasts	CTSL	APOE	M1	IMB
APOE	CST3	IMB	Naïve Tcell	CTSL	CD74	M1	IMB
APOE	CTSL	IMB	M1	COL15A1	CTSB	Cxcl14 FAPs	IMB
APOE	GSN	IMB	Cxcl14 FAPs	COL15A1	CTSS	Cxcl14 FAPs	IMB
APOE	GSN	IMB	Osr1 FAPs	COL4A2	C1QB	Cxcl14 FAPs	IMB
APOE	GSN	IMB	Dpp4 FAPs	C1QA	C1QB	M2	IMB
APOE	HMGB2	IMB	Cd3 Tcell	SLPI	CTSS	Neutrophils	IMB
APOE	HMGB2	IMB	ProliferatingIC	SLPI	CTSB	Neutrophils	IMB
APOE	CTSD	IMB	Ilr7+ Macro	CTSB	CTSD	IMB	Ilr7+ Macro
APOE	PPT1	IMB	Myeloblasts	CTSB	SLPI	IMB	Neutrophils
APOE	S100A8	IMB	Neutrophils	CTSB	SLPI	IMB	Leukocytes
APOE	ALDOA	IMB	SM	CTSB	S100A8	IMB	Neutrophils
APOE	HSPG2	IMB	Cxcl14 FAPs	CTSB	ALDOA	IMB	SM
DCN	C1QA	Osr1 FAPs	IMB	CTSB	APOE	IMB	M2
CD74	CTSB	Mrc1+ Macro	IMB	CTSB	CST3	IMB	Myeloblasts
CD74	CTSS	Mrc1+ Macro	IMB	CTSB	CST3	IMB	Naïve Tcell
C1QB	PTX3	IMB	ActivatedFAPs	C1QA	C1QB	Mrc1 macro	IMB
C1QB	C1QA	IMB	Mrc1+ Macro	MYOC	C1QB	Cxcl14 FAPs	IMB
C1QB	C1QA	IMB	M2	HSPG2	APOE	Cxcl14 FAPs	IMB
C1QB	MYOC	IMB	Cxcl14 FAPs	HSPG2	CTSS	Cxcl14 FAPs	IMB
C1QB	MYOC	IMB	Osr1 FAPs	PROCR	CTSB	Dpp4 FAPs	IMB
C1QB	MYOC	IMB	Dpp4 FAPs	FCER1G	CLEC4E	IMB	Neutrophils

Table S5. Select receptor-ligand pairs enriched between IMB and other populations; related for Figure 5.
Receptor-ligand pairs that show enriched expression between IMB and other clusters.
Abbreviations: FAPs; fibro-adipogenic progenitors, MuSC; muscle satellite cells, IMB; immunomyoblasts, M1; M1-macrophages, M2; M2-macrophages.
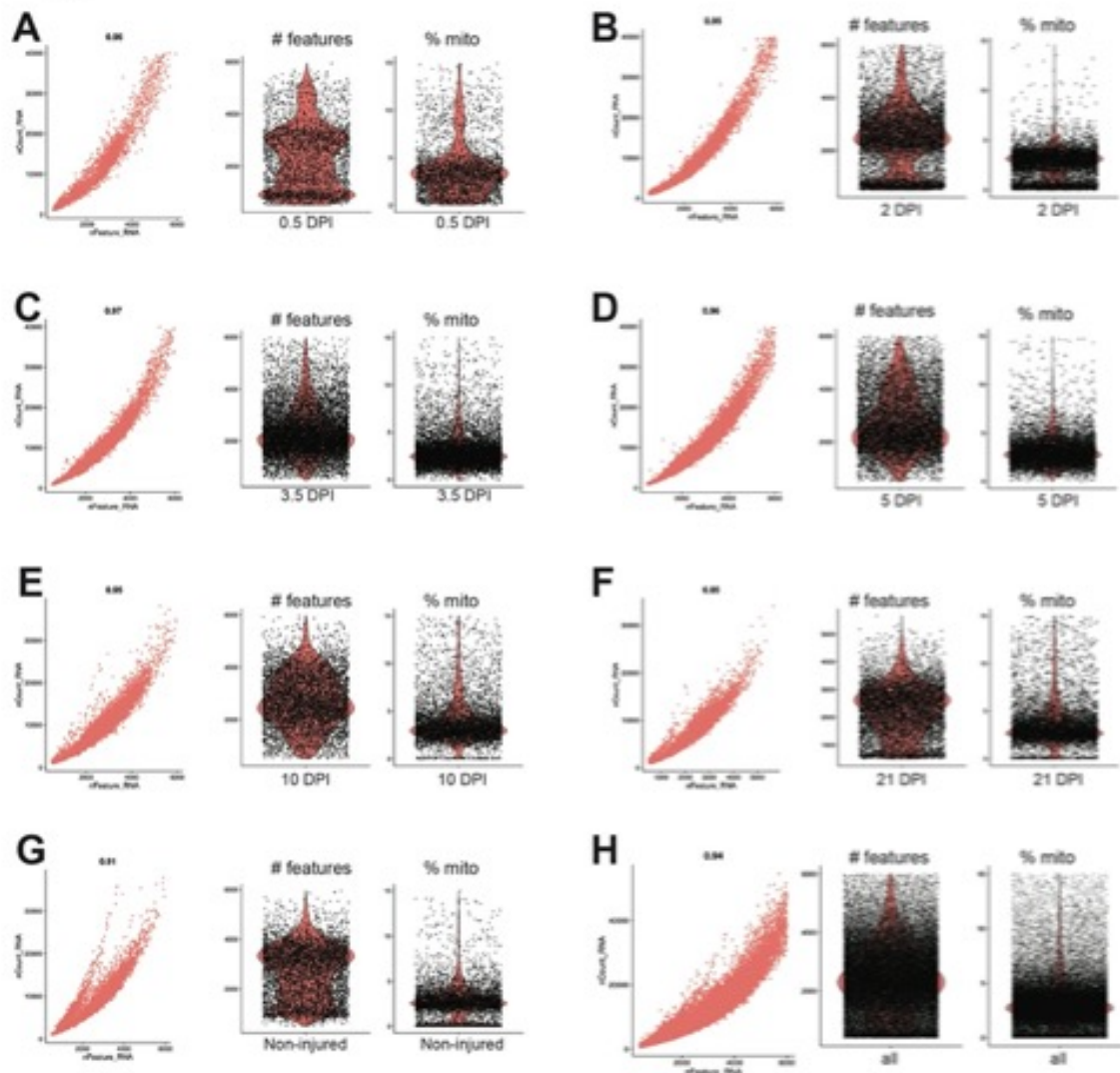
Figure S1. Rationale for selection of time-points and experimental design; related to Figure 1. (A) Summarized events after skeletal muscle injury with cardiotoxin. Along the top are the days post injury (DPI). Red arrow heads are the time points we selected for single-cell transcriptome analysis to capture the most heterogeneity in cell types present. **(B)** Cross-sectioning and hematoxylin & eosin staining of tibialis anterior (TA) muscle at the selected time points during muscle regeneration to confirm features of skeletal muscle regeneration dynamic. **(C)** Overview of experimental design. For each time point and a non-injured control we used 3 male mice 3-4 months of age and dissected the TA muscle. One TA muscle was saved for cross-sectioning and another was digested to isolate mononuclear cells. Samples were stained with a live/dead dye to assess cell viability. Flow cytometry and fluorescence activated cell sorting was used to (1) exclude aggregated cells (2) exclude dead cells and debris. Cells were then counted and processed using 10X Chromium 3' v3 gene expression kit per the manufacturer's instructions.

Figure S2. Quality control metrics for scRNA-seq; related to Figure 1. Scatter plots for each time point show the correlation between number of genes detected (features, X-axis) and number of RNA counts (Y-axis).
Violin plots to show the distribution for the number of features or fraction of mitochondrial RNA. **(A)** 0.5 DPI **(B)** 2 DPI. **(C)** 3.5 DPI. **(D)** 5 DPI. **(E)** 10 DPI. **(F)** 21 DPI. **(G)** Non-injured. **(H)** Aggregate plot containing data from all time points for which the average number of genes detected is 2,348/cell. Abbreviations: DPI; days post injury.
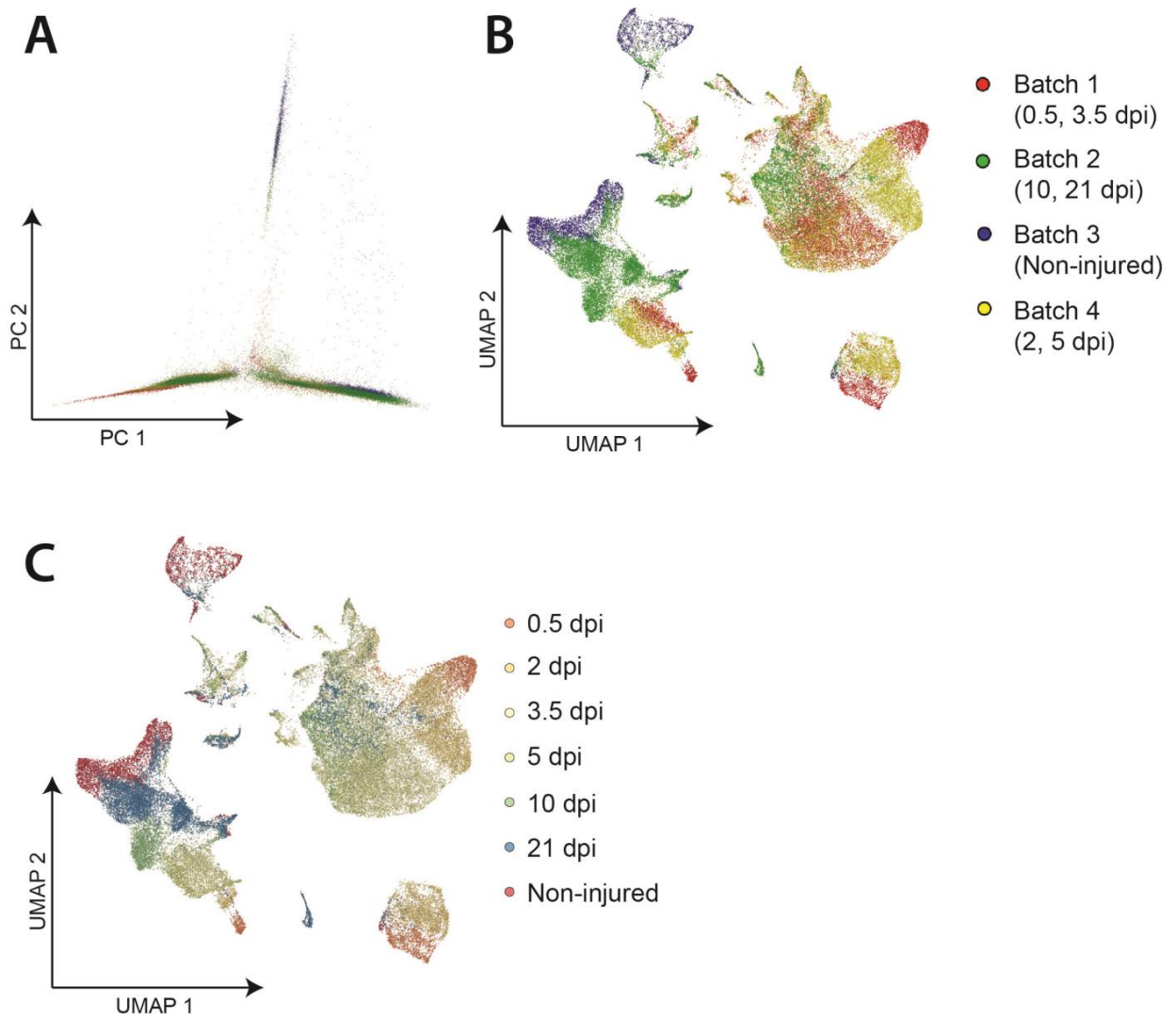
Figure S3. Principal component analysis; related to Figure 1. (A) Principal component analysis of scRNA-seq data colored by batch. **(B)** UMAP embedding of single-cell data, colored by batch. Respective batch colors correspond with the colored dots in both (A) and (B). **(C)** UMAP embedding of single-cell data, colored by time point. Abbreviations: PCA; principal component analysis, DPI; days post injury. UMAP; uniform manifold approximation projection.
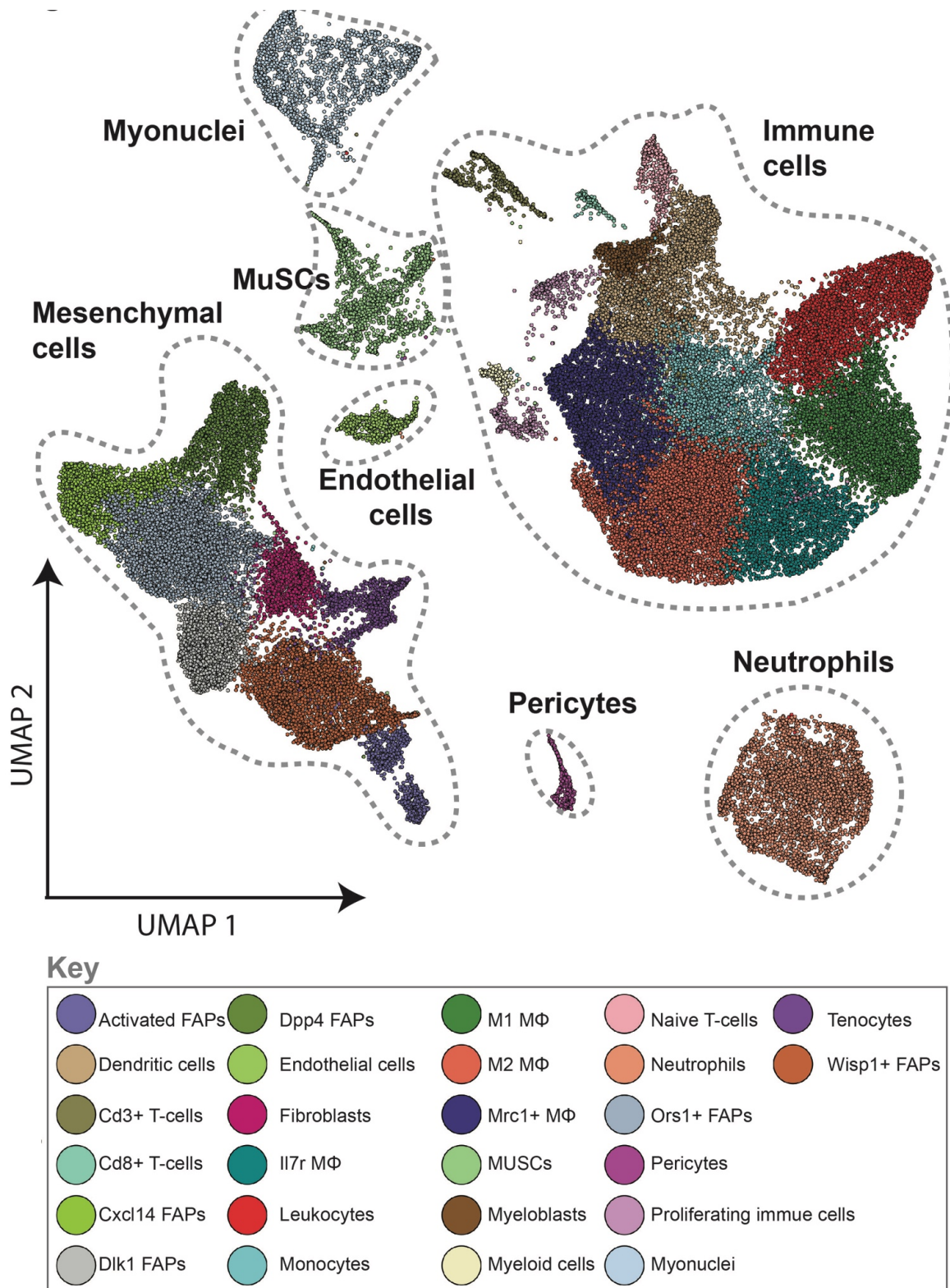
Figure S4. UMAP embedding of all cells colored by cluster; related to Figure 1. Dotted lines represent groups of cells. UMAP embedding colored by individual cluster identities as determined by Louvain clustering and manually annotated based on marker gene expression.

Abbreviations: FAPs; fibro-adipogenic progenitors, MΦ; macrophages.
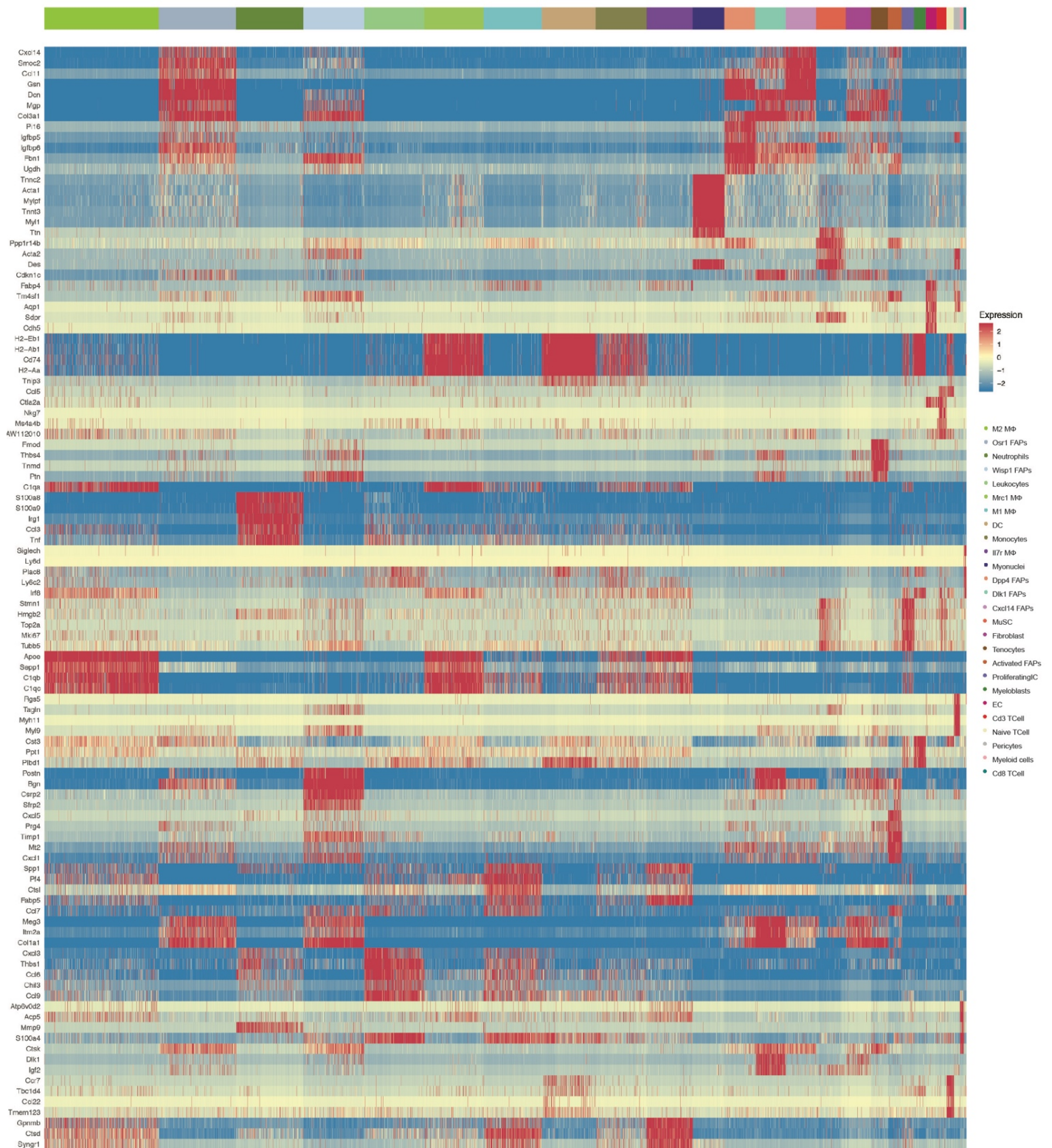
Figure S5. Heatmap for all clusters; related to Figure 1. Heatmap of the top 5 enriched genes per cluster from the merged, complete dataset. Cluster identity is noted along the top (with corresponding cluster identity on the left) of the heatmap and genes are annotated along the left side. Scaled expression values plotted. Abbreviations: FAPs; fibro-adipogenic progenitors, M2: M2 macrophages, M1: M1 macrophages, DC; dendritic cells, SM; skeletal muscle, MuSC; muscle satellite cells, Proliferating IC; proliferating immune cells, EC; endothelial cells.
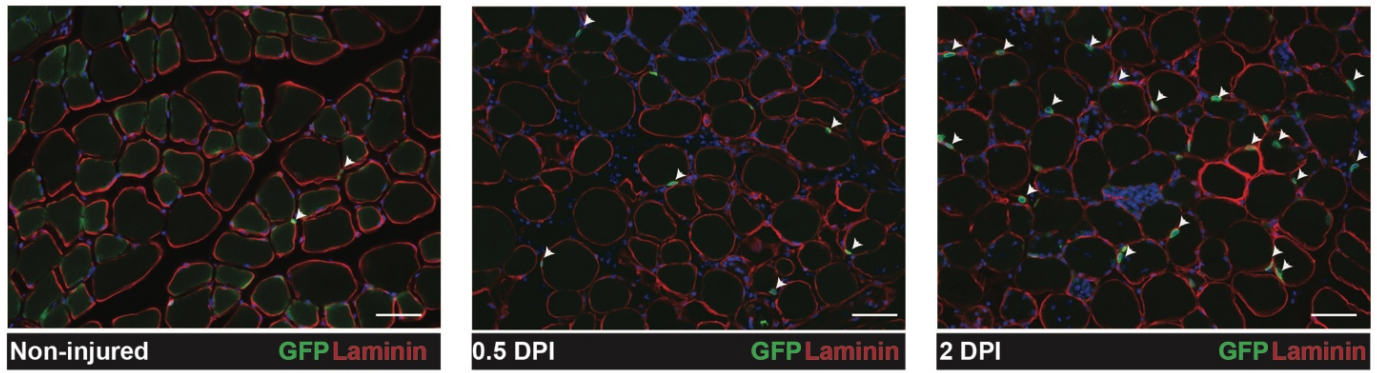
Figure S6. MuSC detection at 0.5- and 2-days DPI by cross-section; related to Figure 1. TAs from Pax7GakaCre+/-;sf-GFP^{+/-} mice were injured with CTX. TA muscles were dissected, cross-sectioned and stained with laminin to visualize myofiber boundary. sfGFP marks MuSCs. Scale bar: 50μm.

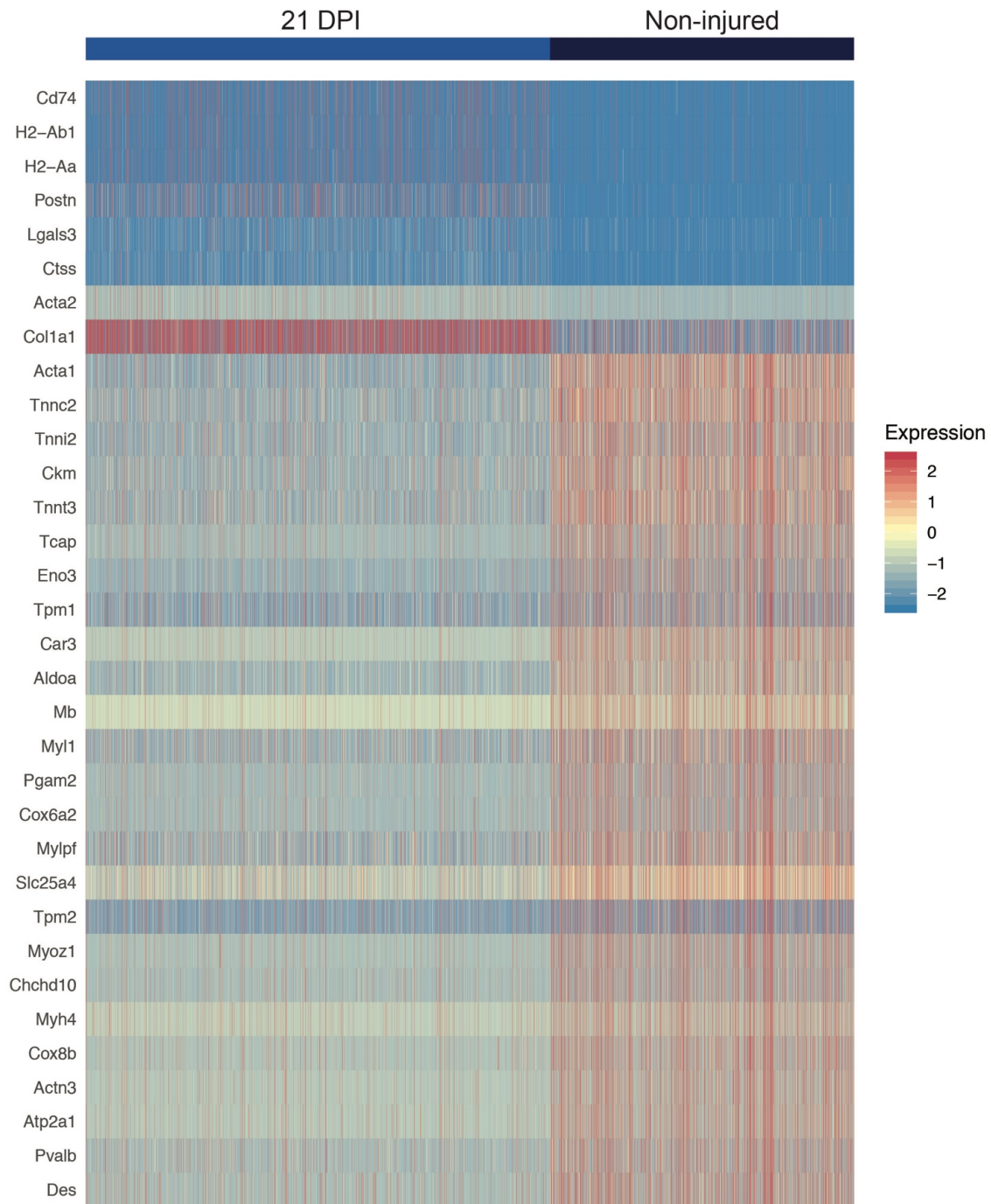Abbreviations: TA; tibialis anterior, DPI; days post injury, CTX; cardiotoxin.

Figure S7. 21 DPI and Non-injured comparisons; related to Figure 1. Heatmap generated by comparison of non-injured and 21 DPI to evaluate transcriptional characteristics differentially expressed across the two samples. Abbreviations: DPI; days post injury.
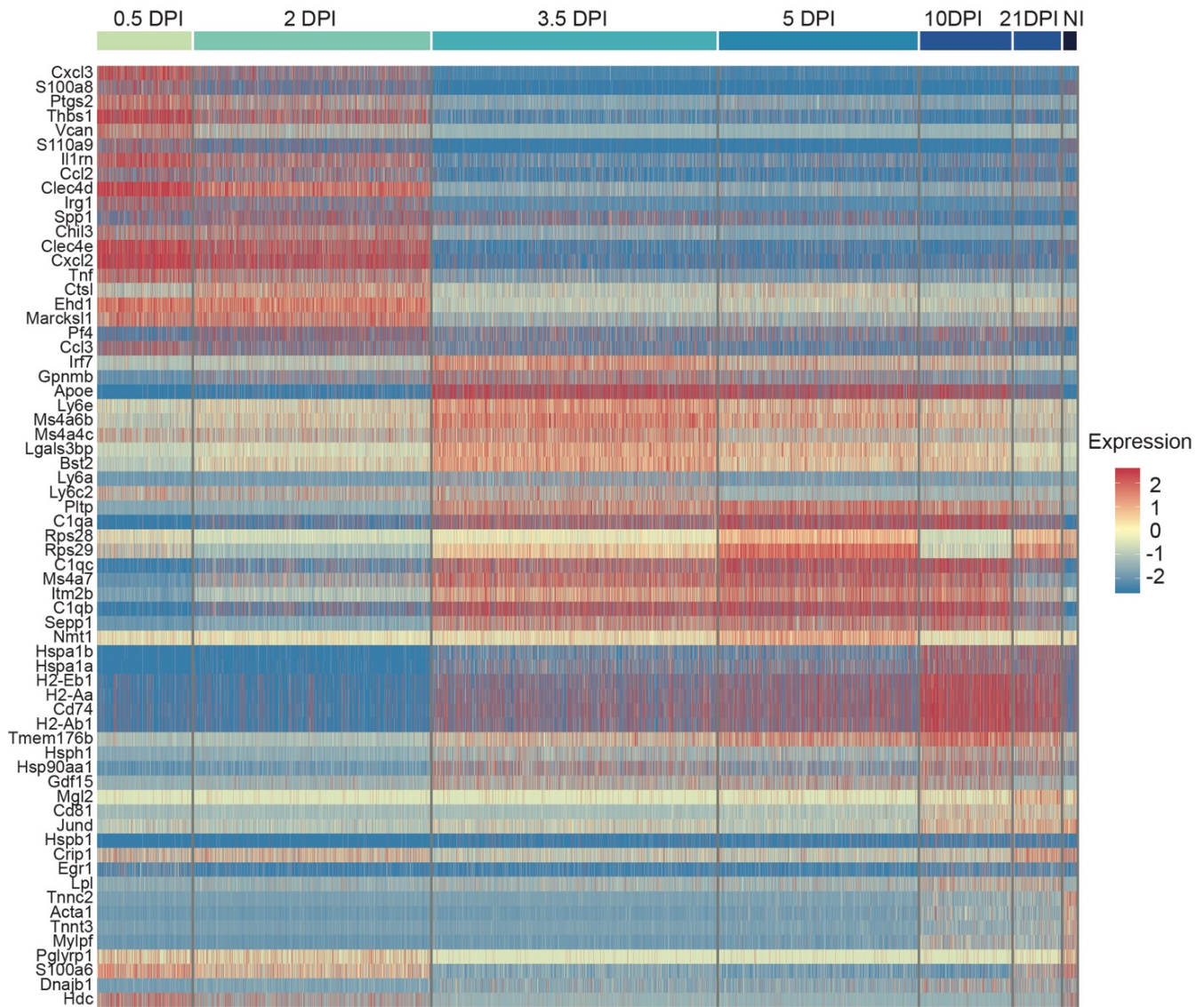
Figure S8. Immune cell time-point specific gene expression signatures; related to Figure 2. Heatmap of the top10 enriched genes as determined by differential gene expression analysis across time points. Cells are grouped by time point and indicated along the top. Clear shift in immune expression characteristics from 2 DPI to 3.5 DPI. Abbreviations: DPI; days post injury.
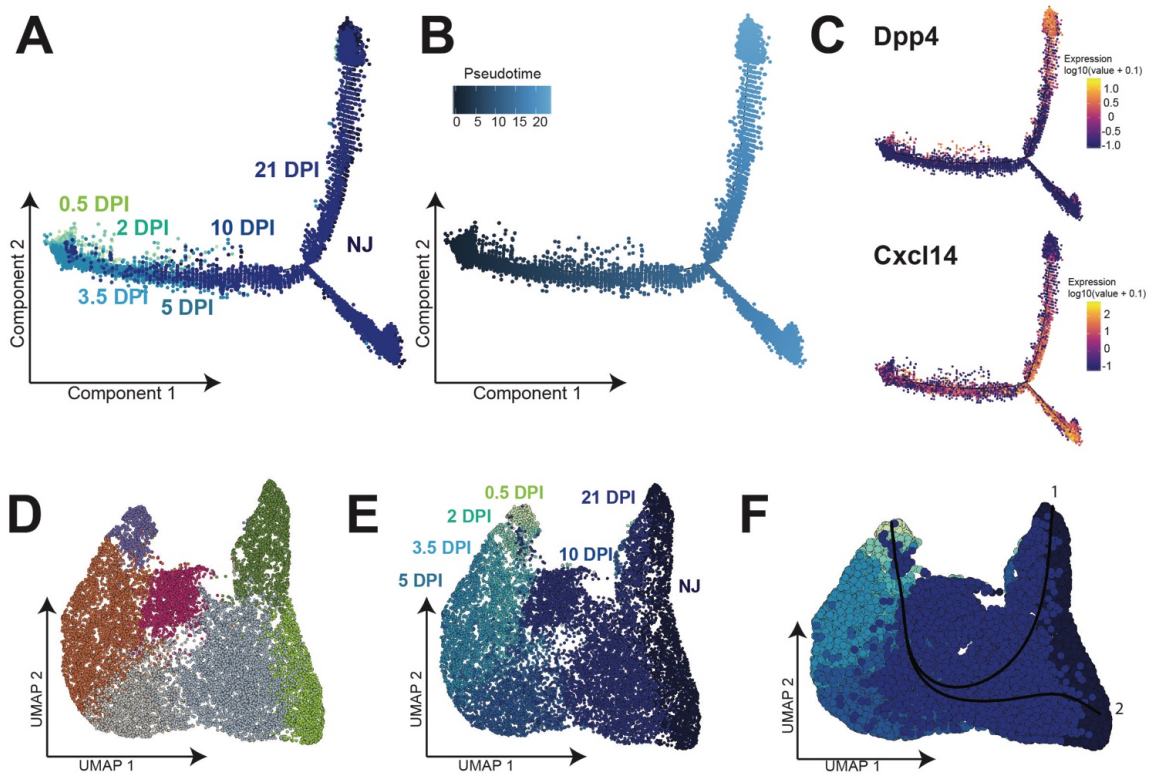
Figure S9. FAP trajectory inference; related to Figure 3. (A) Monocle-derived trajectory of the mesenchymal populations related to Figure 3. Cells along trajectory colored by regeneration time point. **(B)** Monocle trajectory, cells colored by pseudotime. **(C)** Gene expression plots of Dpp4 and Cxcl14 to highlight divergent gene signature of the two subpopulations identified in resting muscle. **(D)** Subclustering of fibroblast and FAP population and UMAP embedding; colored by original cluster identities. **(E)** Sub-clustering of fibroblast and FAP population and UMAP embedding; colored by time point. **(F)** Lineage inference using Slingshot on UMAP embedded subclusters. Black lines are the 2 smoothed lineage curves generated by Slingshot. Colored by time-point.
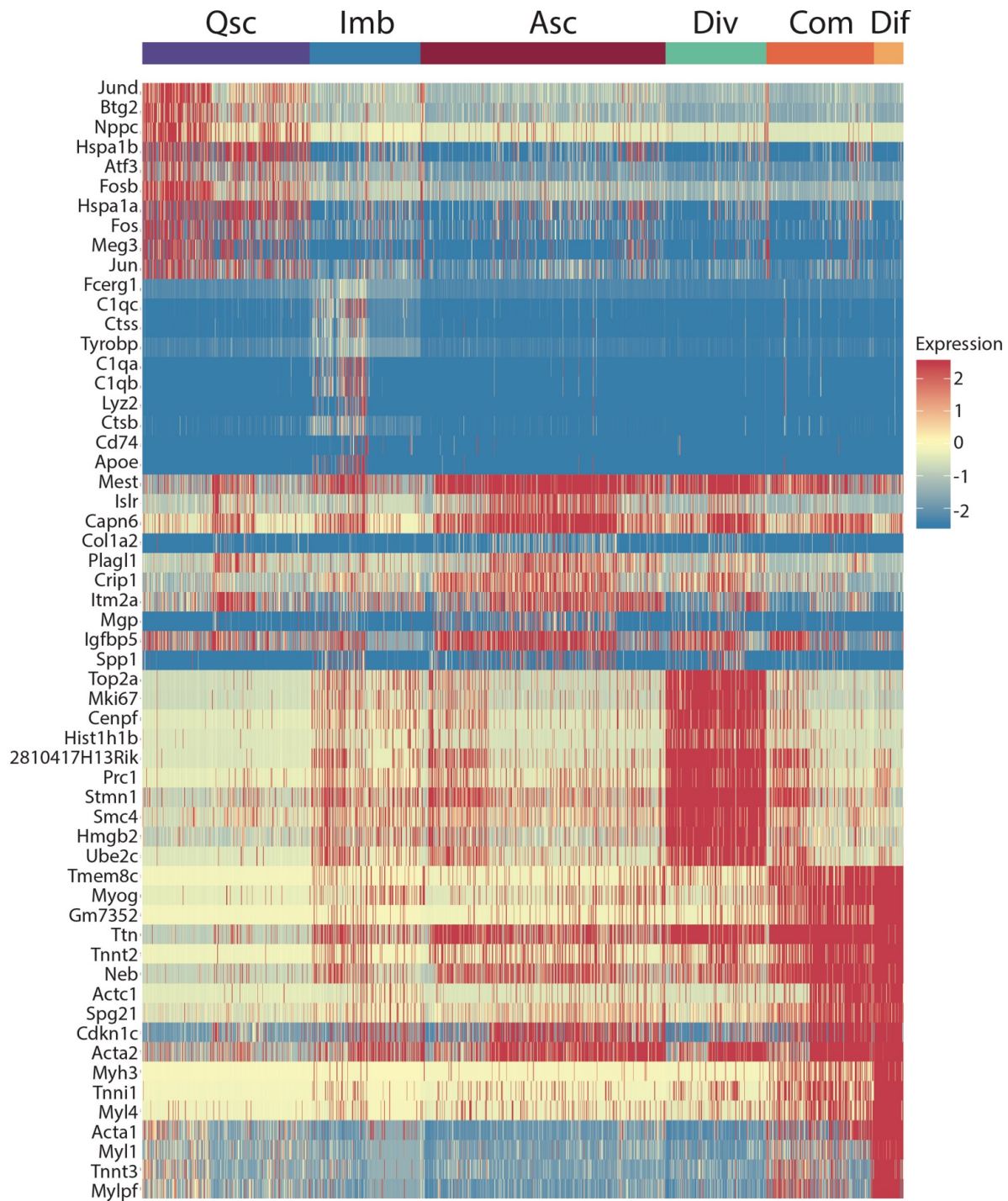Abbreviations: DPI; days post injury, FAPs: fibro-adipogenic progenitors.

Figure S10. Heatmap of sub-clustered MuSC populations; related to Figure 4. Heatmap of top 10 genes as determined by FindAllMarkers() on the subclustered MuSCs. Along the top are the cluster identities. Scaled expression values are plotted.
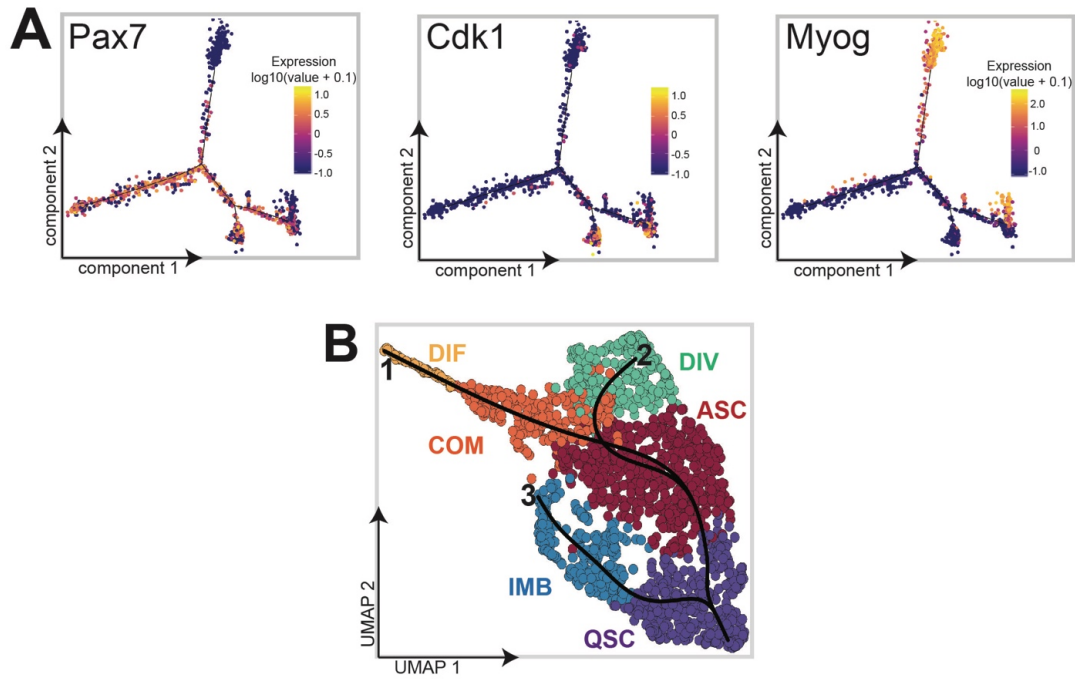
Abbreviations: MuSC; muscle satellite cells.

Figure S11. MuSC trajectory analysis; related to Figure 4. (A) Monocle-derived trajectory of the MuSCs population across regeneration time-points. Gene expression plots for *Pax7*, *Cdk1* and *Myog* to highlight their expression in pseudotime. **(B)** Trajectory inference using Slingshot on the subclustered MuSC UMAP embedding generated 3 smoothened lineage curves.

Abbreviations: Qsc; quiescent, Asc; activated, Imb; immunomyoblasts, Div; dividing, Com; committed, Dif; differentiated.
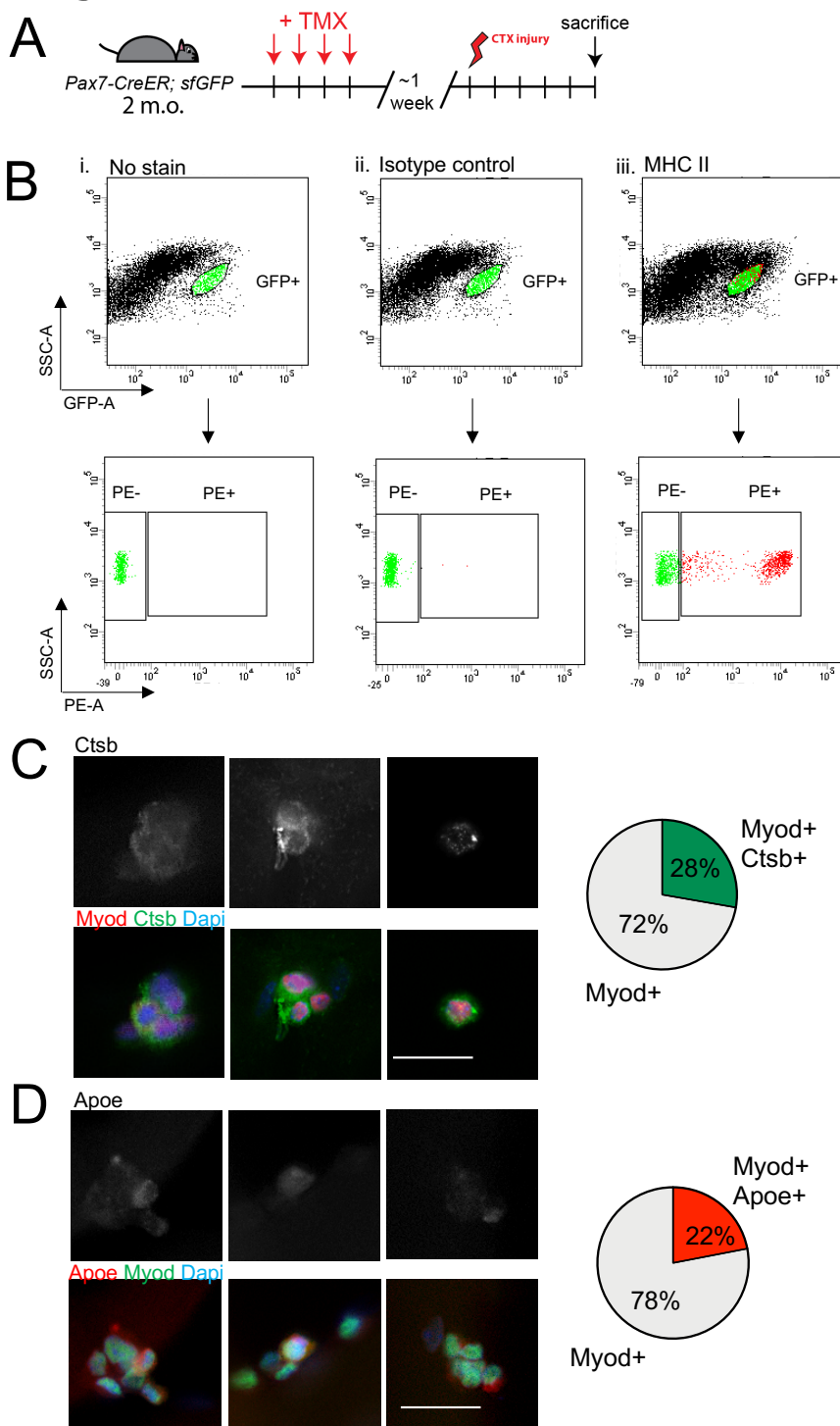
Figure S12. Flow-cytometry and immunofluorescence to evaluate immune-gene expression in MuSCs; related to Figure 5. **(A)** Schematic of tamoxifen-injection to drive the expression of nuclear-membrane GFP in Pax7-positive cells and the subsequent progeny. **(B)** Representative image of FACS samples from 5 DPI muscle where cells were first gated for GFP and then gated for PE fluorescence. (i) No stain to gate for GFP+ cells, (ii) isotype control, no signal PE+ detected in the GFP+ gated cells, (iii) MHC-II, PE+ and PE- cells detected in the GFP+ gated cells. **(C)** Myofiber staining with Myod (red) and Ctsb (green) 72 hours after culture. Top panel: Ctsb single channel, bottom panel: merged image with dapi (blue). Quantification is based on n = 173 Myod-positive cells. **(D)** Myofiber staining with Apoe (red) and Myod (green) 72 hours after culture. Top panel: Apoe single channel, bottom panel: merged image with dapi (blue). Quantification is based on n = 173 Myod-positive cells for both (C) and (D). Images selected highlight the expression of Ctsb and Apoe. Scale bar: 25 um.
Abbreviations: GFP; green fluorescent protein, FACS; fluorescence-activated flow cytometry, DPI; days post injury, MuSC; muscle satellite cells.

TRANSPARENT METHODS

Muscle injury for single-cell RNA-sequencing. For each time-point (0.5-, 2-, 3.5-, 5-, 10-, 21-days post injury) as well as the non-injured control 3 wild-type male C5Bl6/N mice at 3-4 months of age were used. The tibialis anterior (TA) muscle of each mouse was injured via intramuscular injection of 50 μL 10μM cardiotoxin. Both TA muscles per time-point/per mouse were injured and the non-injured control was a non while the non-injured control was a completely non-injured.

Sample processing and flow-cytometry. Both TA muscles from each mouse were dissected, one was used for cross-sectioning while the other was used for down-stream digestion and processing (yielding 3 TAs per time-point for scRNA-seq). Samples were prepared for fluorescence activated cell sorting (FACS) as previously described(Liu et al., 2015). Briefly, the TA was dissected, rinsed with 1X PBS, cut into pieces and digested in wash media (F-10 + 10% horse serum + 1X pen/strep) with 2.5 mg/mL collagenase type II (Worthington Biochemical Corporation, Cat#L5004177) for 1 hour at 37°C. The sample was neutralized with 40 mL wash media, centrifuged at 500xg for 5 minutes, and 40 mL of supernatant was removed leaving 8mL of wash media. To this, 1 mL of 1000U/mL stock collagenase type II and 1 mL of 11U/mL dispase (Roche, Cat#04942078001) was added and the samples were incubated at 37°C for 30 minutes. Digested tissue was run through a 20-gauge needle to further dissociate cells, neutralized with 40 mL wash media and spun down at 500xg for 5 mins at room temperature (~22°C). All but 10 mL of supernatant was removed, cells were then resuspended, run through a 40um filter, diluted with 40 mL wash media and subsequently spun down at 500xg for 5 min at room temperature. Cells were then resuspended in 0.1% BSA in 1X PBS and stained with zombie Live/Dead per the manufacturer's instructions [Biolegend, Cat#423113]. Cells were briefly spun down, wash once with 1X PBS and then resuspended in 0.1% BSA in 1X PBS for fluorescence activated cell sorting (FACS). Cells positive for the zombie Live/dead stain indicated dead or dying cells and thus were excluded. 100,000 live cells/sample were sorted and used for downstream processing with the 10X genomics 3' v3 kit for single-cell gene expression.

Single-cell RNA-sequencing. scRNA-sequencing was performed using the 10X Genomics 3' v3 kit, following their protocol targeting recovery of 10,000 cells. Libraries were constructed per the manufacturer's instructions and sequenced using Illumina's NovaSeq platform. Average read depth across the samples was 43,000 reads/cell. Reads were then aligned to the mouse genome mm10/Grcm38 using the CellRanger 2.1.0 software. Subsequent analysis was performed in R using the filtered barcode and count matrices produced by CellRanger.

Quality control, dimensionality reduction, and visualization. Seurat 3.1.0 was used to analyse the single-cell data(Stuart et al., 2019). All time-points were initially merged together and filtered for quality control parameters (cells with more than 15% reads mapping to mitochondrial genes, feature counts greater than 6,000 and more than 60,000 reads were filtered out; Fig. S2). Seurat's SCTransform function was used to normalize and scale the data to minimize batch effects(Hafemeister and Satija, 2019). Dimensionality reduction was performed through Principal Component Analysis (PCA) following Seurat's tutorial as evaluated by elbow plots (Butler et al., 2018; Hafemeister and Satija, 2019; Satija et al., 2015). UMAP embedding parameters were based on the top 30 PCs and embedded in 2-dimensions for visualization.

Differential gene expression and cell type classification. The clusters identified were evaluated for marker gene expression to determine cell types. Seurat's FindAllMarkers function was used to identify differentially expressed genes (DEGs) per cluster and then manually annotated based on enriched gene expression. All genes considered for cell-type classification had a *P*-value of less than 0.0001 using a Mann-Whitney Wilcoxon test(Stuart et al., 2019).

Sub-cluster analysis. To perform the sub-clustering, we used Seurat's subset function to extract the cell types of interest (MuSCs and FAPs). We then performed subsequent dimensionality reduction, clustering and UMAP visualization in Seurat. We also extracted the raw RNA counts for each assayed cell type to subset, re-scaled the data using the SCTransform function, performed dimensionality reduction, clustering and UMAP visualization and found that both produced similar results (data not shown).

Trajectory inference and analysis. Monocle version 2 and slingshot were used for pseudotime analysis and trajectory inference(Street et al., 2018; Trapnell et al., 2014). Briefly, we used the raw data from MuSCs and the fibroblast and FAP populations for trajectory inference and fit the data to a negative binomial distribution prior to ordering cells (as was used for SCTransform in Seurat). The top 1,000 DEGs were then used for trajectory inference and analysis. For slingshot, we used the scaled data from the MuSC sub-clustering to map the inferred trajectories onto the UMAP plot coordinates following the published vignette. To identify the genes associated with the 3rd trajectory that leads to the immunomyoblast fate, we evaluated the top 100 genes that change as a function of trajectory 3 and fit a generalized additive model with a loess term to calculate gene expression as a function of pseudotime.

Cross-sectioning and antibody staining. CTX-injured and non-injured TA muscles were dissected, placed O.C.T. (Fisher, 4585) and flash frozen in 2-methyl-butane. Samples were cryosection, fixed with 4% paraformaldehyde (PFA) for 10 minutes at room temperature and washed 3 times with 1X PBS (pH 7.5, 3 mins per wash). Remaining PFA was quenched with 1X glycine (0.375g glycine + 50 mL PBS) for 10 mins at RT, samples were washed 3 times with 1X PBS and then blocked for 1 in hour at RT in blocking buffer (1% goat serum, 2% BSA, 0.2% Triton X100, 0.1% sodium azide in 1X PBS), followed by 1 hour blocking in mouse-on-mouse blocking buffer(40µL Mouse IgG blocking reagent (vector lab, MKB-2213) in 1mL 1X PBS). Antibodies (C1q: Invitrogen; PA5-29586, Myod1: Santa-Cruz; sc377460, Apoe: BioLegend; 803404/cloneID E607, Ctsb: 680902/cloneID 15D10C39) were diluted 1:300 and Pax7 antibody (from DSHB) diluted 1:50 in blocking buffer and incubated at 4°C overnight. No primary control was incubated with blocking buffer overnight at 4°C. Samples were washed 3X with 1X PBS at room temperature. Secondary antibodies (568 goat anti-mouse IgG1 (Invitrogen, A21123) and 488 goat anti-rabbit (Invitrogen, A270034) and DAPI were diluted 1:1000 in 1X PBS. Samples were incubated for 1 hour at room temperature, washed 3 times with 1X PBS. For MHC II staining, samples were additionally incubated with MHC-II (1:1000, MHC II (I-A/I-E), ThermoFisher, Catalog # 12-5321-81) and subsequently washed 3X with 1X PBS. Samples were imaged using a Leica DMi6000B microscope at 200X magnification.

Tamoxifen preparation. Tamoxifen (Calbiochem) was dissolved in 100% EtOH to a concentration of 10mg/mL, aliquoted into 2mL microcentrifuge tubes and mixed with equal parts corn oil. Tubes were vacuum centrifuged to evaporate remaining ethanol and stored at -20°C protected from light until use. Mice were injected intraperitonially with 2 mg TMX per 20 g body weight for 4 consecutive days to ensure cre-mediated recombination.

FACS sorting, RNA isolation and qRT-PCR. Pax7^{GakaCreER};sfGFP mice were injected with tamoxifen 4 times (once per day, 4 consecutive days) at 2-3 months of age (male mice, n=3). One side of the hindlimb muscle was injured with CTX and mice were sacrificed and analysed at 5 DPI. Contralateral muscle served as the non-injured control. MuSCs were isolated from muscle tissue as described above (see *Sample processing and flow-cytometry*). For RNA isolation, MuSCs from either non-injured contralateral sample or 5 DPI were sorted based on FITC fluorescence, debris was excluded using live-dead stain. RNA was isolated from sorted cells using PicoPure RNA isolation kit (ThermoFisher, KIT0204) per the manufacturer's instructions. RNA was diluted in 10µL nuclease-free dH$_2$O all of which was used for cDNA and analysis.

cDNA synthesis was carried out using M-MLV Reverse Transcriptase (ThermoFisher, 28025013) following the manufacturer's instructions and diluted 1:5 in nuclease-free dH$_2$O prior to RT-PCR analysis. For RT-PCR analysis each reaction contained 5µL SYBR Green Master Mix (ThermoFisher, 4309155) 0.6µL nuclease-free dH$_2$O, 0.4µL primer mix (forward + reverse, 10 µM), 4µL cDNA. RT-PCR reactions were incubated at (1) 95°C for 30 sec, (2) 95°C 10 sec, 65°C 10 sec, 72°C 10 sec (3) 95°C 10 sec, 65°C 60 sec, 97°C 1 sec, 37°C 30 sec. Step (2) was repeated 30X. Samples were then run on a 1.5% TAE agarose gel and imaged. For MHC II surface expression, MuSCs were isolated from either non-injured or 5 DPI (see *Sample processing and flow-cytometry*) but were also incubated with MHC-II antibody (Catalog # 12-5321-81) or the isotype control (ThermoFisher, Catalog # 12-4031-82) diluted at 1:1000, 4°C for 30 mins. Cells were first gated based on GFP expression and of those, PE positive cells were sorted. After FACS, a drop containing the cell suspension was placed on a cover slide and imaged using a Leica DMi6000B microscope at 200X magnification.

Primer sequences used for RT-PCR

Primer	Forward	Reverse
Actb	5'-GTCACGTTGACATCCGTAAAGA-3'	5'-GCCGCACTCATCGTACTCC-3'
Myog	5'-TGCCCAGTGAATGCAACTCC-3'	5'-TTGGGCATGGTTTCGTCTGG-3'
Pax7	5'-CTGGATGAGGGCTCAGATGT-3'	5'-GGTTAGCTCCTGCCTGCTTA-3'
C1qa	5'-AAAGGCAATCCAGGCAATATCA-3'	5'-TGGTTCTGGTATGGACTCTCC-3'
C1qc	5'-AGAAGCACCAGTCGGTATTCA-3'	5'-TGCGATGTGTAGTAGACGAAGTA-3'
Ctsb	5'-TCCTTGATCCTTCTTTCTTGCC-3'	5'-ACAGTGCCACACAGCTTCTTC-3'
Lyz2	5'-ATGGAATGGCTGGCTACTATGG-3'	5'-ACCAGTATCGGCTATTGATCTGA-3'

Cell-cell interaction networks. To generate inferred interaction networks, we used a published receptor-ligand interaction set (Ramilowski et al., 2015) and the gene signatures for each population as generated by Seurat's FindAllMarkers() function. We first used the cell populations identified at each time-point and filtered for genes with an average log-fold change greater than 1.2 before receptor-ligand pair analysis. We then plotted the sum of the number of receptor-ligand pairs between two cell populations to show a graph that encompasses all cell types. The same analysis was performed for the immunomyoblast population however the interactions were not limited by time-point.

SUPPLEMENTAL REFERENCES

Butler, A., Hoffman, P., Smibert, P., Papalexi, E., and Satija, R. (2018). Integrating single-cell transcriptomic data across different conditions, technologies, and species. Nat. Biotechnol. *36*, 411–420.

Hafemeister, C., and Satija, R. (2019). Normalization and variance stabilization of single-cell RNA-seq data using regularized negative binomial regression. BioRxiv 576827.

Liu, L., Cheung, T.H., Charville, G.W., and Rando, T.A. (2015). Isolation of skeletal muscle stem cells by fluorescence-activated cell sorting. Nat. Protoc. *10*, 1612–1624.

Ramilowski, J.A., Goldberg, T., Harshbarger, J., Kloppmann, E., Lizio, M., Satagopam, V.P., Itoh, M., Kawaji, H., Carninci, P., Rost, B., et al. (2015). A draft network of ligand–receptor-mediated multicellular signalling in human. Nat. Commun. *6*, 7866.

Satija, R., Farrell, J.A., Gennert, D., Schier, A.F., and Regev, A. (2015). Spatial reconstruction of single-cell gene expression data. Nat. Biotechnol. *33*, 495–502.

Street, K., Risso, D., Fletcher, R.B., Das, D., Ngai, J., Yosef, N., Purdom, E., and Dudoit, S. (2018). Slingshot: cell lineage

and pseudotime inference for single-cell transcriptomics. BMC Genomics *19*, 477.

Stuart, T., Butler, A., Hoffman, P., Stoeckius, M., Smibert, P., Satija, R., Hafemeister, C., Papalexi, E., Mauck Iii, W.M., and Hao, Y. (2019). Comprehensive Integration of Single-Cell Data Resource Comprehensive Integration of Single-Cell Data. Cell *177*.

Trapnell, C., Cacchiarelli, D., Grimsby, J., Pokharel, P., Li, S., Morse, M., Lennon, N.J., Livak, K.J., Mikkelsen, T.S., and Rinn, J.L. (2014). The dynamics and regulators of cell fate decisions are revealed by pseudotemporal ordering of single cells. Nat. Biotechnol. *32*, 381–386.